

Cryo-EM structures of the active NLRP3 inflammasome disc

<https://doi.org/10.1038/s41586-022-05570-8>

Le Xiao^{1,2}, Venkat Giri Magupalli^{1,2} & Hao Wu^{1,2}✉

Received: 16 October 2022

Accepted: 17 November 2022

Published online: 28 November 2022

 Check for updates

Inflammasomes are cytosolic innate immune complexes that activate caspase-1 following detection of pathogenic and endogenous dangers^{1–5}, and NACHT-, leucine-rich repeat (LRR)- and pyrin domain (PYD)-containing protein 3 (NLRP3) is an inflammasome sensor of membrane damage highly important in regard to the induction of inflammation^{2,6,7}. Here we report cryogenic electron microscopy structures of disc-shaped active NLRP3 oligomers in complex with adenosine 5'-O-(3-thio)triphosphate, the centrosomal NIMA-related kinase 7 (NEK7) and the adaptor protein ASC, which recruits caspase-1. In these NLRP3–NEK7–ASC complexes, the central NACHT domain of NLRP3 assumes an ATP-bound conformation in which two of its subdomains rotate by about 85° relative to the ADP-bound inactive conformation^{8–12}. The fish-specific NACHT-associated domain conserved in NLRP3 but absent in most NLRPs¹³ becomes ordered in its key regions to stabilize the active NACHT conformation and mediate most interactions in the disc. Mutations on these interactions compromise NLRP3-mediated caspase-1 activation. The N-terminal PYDs from all NLRP3 subunits combine to form a PYD filament that recruits ASC PYD to elicit downstream signalling. Surprisingly, the C-terminal LRR domain and the LRR-bound NEK7 do not participate in disc interfaces. Together with previous structures of an inactive NLRP3 cage in which LRR–LRR interactions play an important role^{8–11}, we propose that the role of NEK7 is to break the inactive cage to transform NLRP3 into the active NLRP3 inflammasome disc.

NACHT-, leucine-rich repeat (LRR)- and pyrin domain (PYD)-containing protein 3 (NLRP3) belongs to the NLR family and is a versatile inflammasome sensor that detects a range of pathogenic invasions and damage-associated stimuli including the bacterial toxin nigericin, extracellular ATP, amyloid-β fibrils and uric acid crystals. These stimuli converge to cellular K⁺ efflux, a common trigger for NLRP3 activation^{2,14}. The fish-specific NACHT-associated (FISNA) domain of NLRP3, between the PYD and NACHT domains (Fig. 1a), has been implicated as a conformational switch in NLRP3 activation following induction of K⁺ efflux using a cellular bioluminescence resonance energy transfer assay¹³. Previous studies also suggest that, following triggering, NLRP3 traffics on transGolgi network (TGN) marker-containing vesicles along the microtubule to the microtubule organizing centre (MTOC)^{15–17}. Activated NLRP3 recruits ASC, which is the adaptor apoptosis-associated speck-like protein containing a caspase recruitment domain (CARD), through PYD–PYD interactions, and ASC in turn recruits and activates caspase-1 through CARD–CARD interactions^{18–21} to form the NLRP3 inflammasome as a singular speck at the MTOC^{15,17}. Intriguingly, centrosomal NIMA-related kinase 7 (NEK7), important in mitosis, has been identified as a scaffolding protein in NLRP3 activation independent of its kinase activity^{22–24}. Activated caspase-1 cleaves the proinflammatory cytokines pro-IL-1β and pro-IL-18 and the pore-forming protein gasdermin D (GSDMD) to mediate mature cytokine release and pyroptotic cell death^{25–32}. NLRP3 mutations cause autoinflammatory diseases^{33,34},

and NLRP3 hyperactivation is associated with many common conditions including cardiovascular, metabolic and neurodegenerative diseases^{2,35}. Our structures of the NLRP3–NEK7–ASC complex in the active state shed light on NLRP3 inflammasome assembly and activation to mount host defences and restore cellular homeostasis, and provide a platform for understanding and targeting NLRP3-related human diseases.

Structure determination

We co-expressed full-length NLRP3 and NEK7 (Fig. 1a) in Expi293F cells, stimulated the cells with nigericin—a known NLRP3 activator that we used previously¹⁵—and purified the NLRP3–NEK7 complex using the FLAG tag on NEK7. Gel filtration chromatography showed two peaks, but neither gave rise to large homogeneous particles under negative-staining EM (Extended Data Fig. 1a–c). Because ATP was reported previously as essential for activation of the NLRP3 inflammasome³⁶, we added the ATP analogue adenosine 5'-O-(3-thio)triphosphate (ATPyS) and MgCl₂ with the goal of locking NLRP3 in an active conformation. Gel filtration chromatography of the NLRP3–NEK7 complex in the presence of ATPyS showed larger complexes but the sample remained heterogeneous (Extended Data Fig. 1d–h). We wondered whether ASC is required for assembly of the NLRP3 inflammasome, and thus expressed and purified the PYD of ASC (Fig. 1a) as described

¹Department of Biological Chemistry and Molecular Pharmacology, Harvard Medical School, Boston, MA, USA. ²Program in Cellular and Molecular Medicine, Boston Children's Hospital, Boston, MA, USA. ✉e-mail: wu@crystal.harvard.edu

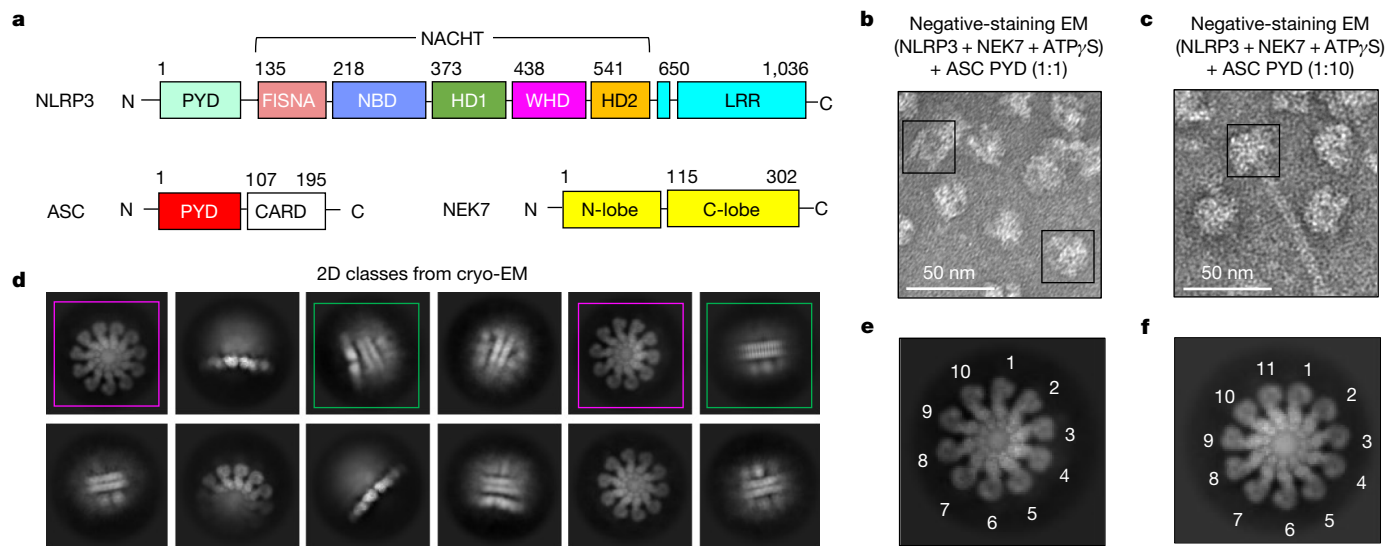


Fig. 1 | Preparation and characterization of the NLRP3–NEK7–ASC inflammasome complex. **a**, Domain organizations of human NLRP3, NEK7 and ASC. Approximate domain boundaries are labelled. **b**, Representative negative-staining EM image from a purified sample containing NLRP3, NEK7, ATP γ S and 1:1 ASC PYD. A stacked NLRP3–NEK7 complex (left) and a single NLRP3–NEK7–ASC complex (right) are enclosed by two black squares. **c**, Representative negative-staining EM image from a purified sample similar to

that in **b** but containing tenfold excess ASC PYD. An NLRP3–NEK7–ASC complex with a long ASC filament is indicated by the black square. **b,c**, Experiments were repeated at least three times. **d**, 2D classes from cryo-EM images of the sample in **b**. Magenta squares indicate examples of top/bottom views of complete discs, and green squares highlight the central NLRP3 PYD filament from stacked discs. **e,f**, Enlarged views of tenfold (**e**) and 11-fold (**f**) 2D classes from **d**.

previously¹⁸. We then added ASC PYD to the NLRP3–NEK7 complex at a 1:1 molar ratio. The mixture was incubated overnight with tobacco etch virus protease to remove the maltose-binding protein (MBP) tags on NLRP3 and ASC PYD, and was then subjected to gel filtration chromatography. The sharp peak near the void elution position contained all three proteins although ASC PYD appeared to be substoichiometric, probably because of the precipitation of large ASC PYD filaments or its retention by the filter membrane in the gel filtration column (Extended Data Fig. 2a–c). Negative-staining EM showed largely homogeneous particles of around 30 nm in diameter (Fig. 1b), suggesting that ASC PYD co-assembles with NLRP3 to complete its activation. Addition of ASC PYD to the NLRP3–NEK7 complex at a 10:1 overstoichiometric molar ratio resulted in some particles having long filamentous tails (Fig. 1c), which confirms the ability of the NLRP3 inflammasome we reconstituted to nucleate ASC PYD polymerization.

We collected cryogenic electron microscopy (cryo-EM) data on the NLRP3–NEK7–ASC complex (Extended Data Fig. 2d). Two-dimensional (2D) classification showed full discs on top/bottom views (Fig. 1d), each containing ten or 11 subunits (Fig. 2e–f). We solved cryo-EM structures of the tenfold disc (C10) at 3.4 Å resolution, and of the 11-fold (C11) disc at 3.8 Å resolution (Extended Data Figs. 3 and 4a,b and Extended Data Table 1). Local-resolution distributions showed that the centre of the discs, which represents the key region for NLRP3 oligomerization, had the best resolution of around 2.8 Å (Extended Data Fig. 4a). Some of the complexes are partial discs, as shown by 2D classification (Fig. 1d), and three-dimensional reconstruction using particles from these classes resulted in a cryo-EM map containing mainly five subunits at 3.8 Å resolution (Extended Data Figs. 3 and 4c and Extended Data Table 1).

We observed tubular density for the PYD filament of NLRP3 and ASC from side views of the C10 and C11 maps (Extended Data Fig. 5a,b); the density, however, was weak, probably because of the different symmetry of the filament from the rest of the domains, and the flexible linker after the PYD. The five-subunit map showed only diffuse density in this region (Extended Data Fig. 5c), suggesting that more subunits in a disc may be required for effective recruitment of ASC by nucleation of ASC PYD filament formation. Because some particles contain stacked discs

(Fig. 1b), which are linked together by the NLRP3 PYD filaments from the opposing discs, the 2D classes showed a longer PYD filament in the middle (Fig. 1d), from which we obtained a 3.3-Å-resolution structure of the NLRP3 PYD filament by helical reconstruction (Extended Data Figs. 3 and 5d and Extended Data Table 1). This NLRP3 filament structure is similar to that published previously¹⁰.

Because of enhanced resolution, we will focus on the atomic model built for the C10 disc of the active NLRP3 inflammasome consisting of ten full-length NLRP3 and ten full-length NEK7, using previous NLRP3 (ref.⁸) and full-length NEK7 (ref.³⁷) structures as initial models. In addition, approximately 20 PYD subunits in a filament fit well with the height of the central tubular density visible from the side view of the disc, and we thus built a cofilament consisting of ten NLRP3 PYD and ten recruited ASC PYD¹⁸ to complete the NLRP3–NEK7–ASC complex. Representative regions of cryo-EM density superimposed with the final C10 model are shown in Extended Data Fig. 6.

Overall structure of the NLRP3 disc

The cryo-EM structure showed that the individual NLRP3 subunit consists of the flexibly linked N-terminal PYD, the FISNA domain¹³, the canonical NACHT domain comprising the ATP γ S-bound nucleotide-binding domain (NBD), helical domain 1 (HD1), a winged helix domain (WHD) and helical domain 2 (HD2) and the C-terminal LRR domain (Figs. 1a and 2a). Ten such subunits form a large flower-shaped disc of diameter about 32 nm from top and bottom views, in which the FISNA–NACHT domains interact near the centre of the disc and the LRR domains and bound NEK7 extend away from the centre (Fig. 2b–e). Thus, neither NEK7 nor the NLRP3 LRR domain participates in direct interactions in the disc assembly. At the FISNA–NACHT region of the assembly, the top view shows prominent NBD, WHD and HD2 whereas the bottom view shows more prominent FISNA and HD1 (Fig. 2b). The acidic loop (residues 686–725) situated at the LRR–LRR interface in a decameric cage structure of human NLRP3 (ref.¹⁰) but disordered in all other human and mouse NLRP3 structures^{8,9,11}, is also disordered in the activated NLRP3 structure. The side view of the disc highlights the NLRP3–ASC PYD cofilament complex (Fig. 2c,d).

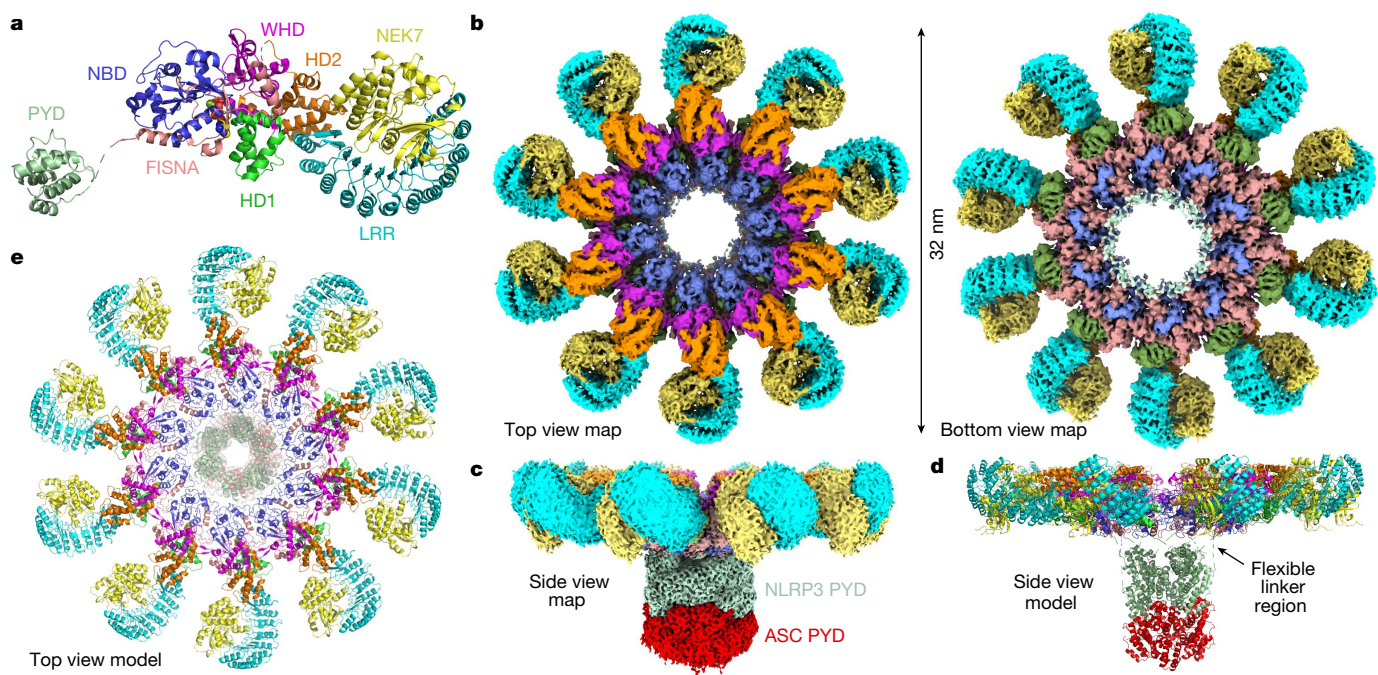


Fig. 2 | Cryo-EM structure of the C10 NLRP3–NEK7–ASC inflammasome complex. **a**, An NLRP3–NEK7 subunit coloured by domains as in Fig. 1a. The position of the PYD is somewhat arbitrary because of the disordered linker. The bound Mg–ATP γ S is shown in spheres with Mg $^{2+}$ in lemon green, carbon atoms in yellow, oxygen atoms in red, nitrogen atoms in blue and sulfur atoms in bright orange. **b**, Top and bottom views of the C10 NLRP3–NEK7–ASC complex

cryo-EM map coloured by domains. **c**, Side view of the C10 NLRP3–NEK7–ASC complex cryo-EM map, highlighting the density for ten NLRP3 PYD and ten ASC PYD. **d**, Side view of the C10 NLRP3–NEK7–ASC complex model, coloured by domains. **e**, Top view of the model of the C10 NLRP3–NEK7–ASC complex, also in domain colours.

Conformational change at FISNA and NACHT

The conformation of active NLRP3 shows marked differences from those of inactive NLRP3 solved in PYD-deleted form in complex with NEK7 (ref. ⁸), in full-length cage forms^{9–11}, in PYD-deleted hexameric form¹¹ or in NACHT alone in complex with an inhibitor¹². When the FISNA–NBD–HD1 regions of NLRP3 in the two states are aligned, the WHD–HD2–LRR module needs to rotate by approximately 85.4° along an axis at the junction between HD1 and WHD to turn from the inactive to the active state (Fig. 3a). This structural change is roughly a rigid body rotation because the FISNA–NBD–HD1 and WHD–HD2–LRR modules align well in gross conformations between the inactive and active states (Fig. 3b and Extended Data Fig. 7a). At the overall structural level, the LRR domain and NEK7 of the inactive NLRP3–NEK7 complex would have been in conflict with a neighbouring NLRP3 molecule in the active disc (Extended Data Fig. 7b).

In NLRC4, the only example among NLRs for which both inactive and active structures are available, the WHD–HD2–LRR module needs to rotate by about 87.5° along a similar axis to change from the inactive state to active^{38–40}. Whereas rotations in NLRP3 and NLRC4 are quite similar, the active states of NLRP3 and NLRC4 are considerably different (Extended Data Fig. 7c), resulting in inaccurate modelling of the active NLRP3 disc⁸ from the known structure of the NLRC4 disc^{38,39}.

The exception to rigid body rotation in conformational change is the FISNA domain, which undergoes pronounced structural changes (Fig. 3c). A region in the middle of the FISNA domain disordered in the inactive conformation becomes an α -helix (helix 2, residues 176–202), and disordered loop 1 (residues 151–163) becomes ordered in the active conformation (Fig. 3c). The disorder of helix 2 and loop 1 in the inactive conformation is because of conflict with LRR–NEK7 and WHD, respectively, if these regions were ordered (Fig. 3d). In addition, loop 2 (residues 212–217) undergoes conformational change (Fig. 3c). These structural changes indicate that the FISNA domain plays an important

role in the activation of NLRP3. Whereas the presence of FISNA is unique to NLRP3 and NLRP12 among NLRPs¹³, structural alignment showed that NLRC4 and NAIP5 (refs. ^{41,42}) also have a FISNA domain that is, however, similar to the inactive conformation of the NLRP3 FISNA domain, with a deletion of helix 2 (Extended Data Fig. 7d).

ATP binding and NLRP3 disease mutations

Conformational changes at the FISNA and NACHT domains are accompanied by exchange of ADP in the inactive conformation to ATP γ S (mimicking ATP) in the active conformation. Whereas the cryo-EM density for ATP γ S is clear (Extended Data Fig. 6h), that for Mg $^{2+}$ is weak for reasons unknown. In the active state, ATP γ S is surrounded mainly by NBD but also by FISNA and, more peripherally, by HD1 and WHD (Fig. 3e). For NBD, certain main-chain amide nitrogen atoms of the Walker A motif⁴³ (or P-loop, 226-GAAGIGKTI-234), and the side chains of K232 of the Walker A motif and R351 of the sensor 1 motif⁴³ (346-LLITTR-351), interact with the phosphate groups of ATP γ S. D302 of the Walker B motif⁴³ (298-LFLMDGFDE-306) helps in coordinating the bound Mg $^{2+}$ ion with β - and γ -phosphates. For the FISNA domain, R154 (loop 1) forms a hydrogen bond with the O₃ atom of the ribose, and T169 main and side chains interact with N₁ and N₆ atoms of the adenine ring. If ATP is placed in the ADP-bound, inactive state, the conserved H522 residue in WHD—important for ADP binding—would come into conflict with ATP γ S (Fig. 3f), rationalizing the required change in WHD location in the ATP-bound, active state.

Although it has been speculated that all NLRs can switch between an ADP-bound inactive conformation and an ATP-bound active conformation, there has not been any structural observation of both states other than that observed here in NLRP3. For NLRC4, the only example among NLRs for which both inactive and active structures are available, no bound nucleotide was captured in the active state although the inactive state binds ADP^{38–40}. In the NLR-related protein Apaf-1, the

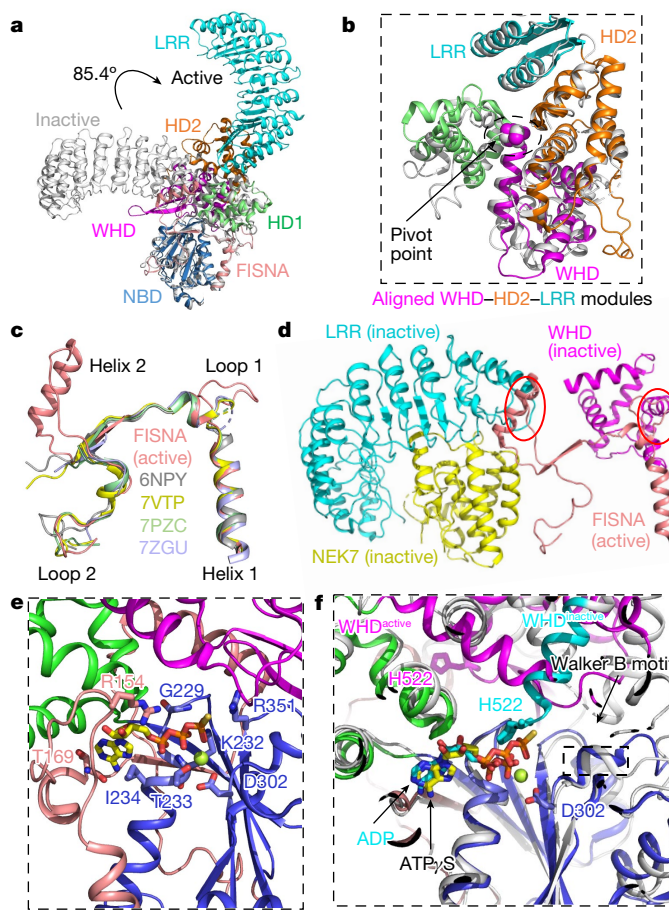


Fig. 3 | Conformational activation of the NLRP3 inflammasome.

a, Superposition of active NLRP3 (in domain colours) and inactive NLRP3 (PDB: 6NPY in grey) by the FISNA–NBD–HD1 segment, showing overall similarity in the FISNA–NBD–HD1 region and rigid body rotation of the WHD–HD2–LRR segment. **b**, Superposition of active NLRP3 (in domain colours) and inactive NLRP3 (grey) by the WHD–HD2–LRR segment, showing overall similarity in this region. **c**, The active FISNA domain aligned with those in inactive NLRP3 structures (PDB: 6NPY, 7VTP, 7PZC and 7ZGU), showing the ordering of loop 1 and helix 2 and the conformational change at loop 2. **d**, Loop 1 and helix 2 in the active FISNA domain clash with WHD and LRR, respectively, in the inactive state. **e**, ATPyS interacts with both the FISNA domain and NBD. Mg²⁺ is shown in lemon green. **f**, Superposition of active NLRP3 and inactive NLRP3 (PDB: 6NPY in grey and cyan) showing the positions of ATPyS (carbon atoms in yellow) and ADP (carbon atoms in cyan), respectively. H522 of the WHD of inactive NLRP3 (cyan) would have clashed with the bound ATPyS.

domain rotation at the junction between HD1 and WHD between the two states is around 180° (ref. ⁴⁴) and in CED-4, the Apaf-1 orthologue in *Caenorhabditis elegans*, no conformational change in the ATPase region was observed because the inactive state is already bound to ATP but oligomerization is prevented by the bound inhibitor CED-9 (refs. ^{45,46}).

To investigate the mechanism of NLRP3-related autoinflammation, we mapped disease mutations in cryopyrin-associated periodic syndromes (CAPS)³⁴—familial cold autoinflammatory syndrome 1, Muckle–Wells syndrome and chronic infantile neurologic cutaneous and articular syndrome—onto the active NLRP3 structure (Extended Data Fig. 8a,b). Within the FISNA domain, residue I174 at the I174T mutation site interacts with the NBD and engages the V200 residue at the V200M mutation site that was disordered in the inactive conformation; both I174 and V200 can stabilize the FISNA domain in the active conformation. T438I and A441V/T mutations are located at

the beginning of the WHD, near the pivot point for the activation of conformational change, which may cause auto-activation of NLRP3. Similar to a previous report⁸, most other CAPS mutations are located near the nucleotide-binding site in the NBD, including R262W/L/P, L266H, D305N/G, L307P, T350M and A354V. These mutations may either destabilize the inactive conformation or stabilize the active conformation of NLRP3.

FISNA domain at the NLRP3 interface

There are three major elements of interaction at an NLRP3–NLRP3 interface, and we named the two neighbouring NLRP3 molecules A and B to facilitate the analysis—as we did for the NLRC4 inflammasome³⁸ (Fig. 4a–c). First, FISNA loop 1 of NLRP3^A interacts primarily with the NBD and FISNA domain of the neighbouring NLRP3^A. Second, FISNA loop 2 of NLRP3^A interacts with FISNA helix 1 of NLRP3^B. Third, a region in NLRP3^A WHD becomes an ordered β-hairpin loop (Extended Data Fig. 8c) and interacts with NLRP3^B HD1. These interactions have a strong electrostatic component, with the NLRP3^A interaction surface being largely acidic and NLRP3^B interaction surface largely basic (Fig. 4d). By contrast, the corresponding NLRC4^A surface is largely basic and NLRC4^B largely acidic³⁸.

Quantitative analysis using PDBePISA for exploration of macromolecular interfaces⁴⁷ identified FISNA domain residues R147 from helix 1, E152, N155 and R157 from loop 1, D213 from loop 2, K166 and E176 from other regions, NBD residues Q359 and H364, HD1 residue Q424 and WHD residues Q509 and D513 as contributing substantially to the interaction (Fig. 4c). Despite the similarity with NLRP3, NLRC4 uses only the corresponding FISNA loop 1 in oligomerization whereas FISNA loop 2 and the equivalent β-hairpin loop in WHD are barely present in NLRC4 (Extended Data Figs. 7d and 8d). In fact, very different interaction surfaces are used in the NLRP3 and NLRC4 discs; if one of the subunits in a pair of NLRP3 subunits is aligned to that in a pair of NLRC4 subunits, the neighbouring subunit in the NLRC4 pair needs to rotate by around 32° to match the orientation of that in the NLRP3 pair (Extended Data Fig. 8e).

To test the importance of NLRP3 interfacial residues on NLRP3 inflammasome activation, we generated charge reversal and alanine mutations on these residues (Fig. 4e). We then reconstituted wild-type (WT) and mutant human NLRP3 into NLRP3^{-/-} mouse immortalized bone marrow-derived macrophages (iBMDMs) to examine the response following NLRP3 stimulation. We previously used this system successfully to examine the NLRP3–NEK7 interface in NLRP3 inflammasome activation⁸. Following priming by Toll-like receptor (TLR) ligand lipopolysaccharides (LPS) and stimulation by nigericin, WT NLRP3-reconstituted NLRP3^{-/-} iBMDMs activated caspase-1, as shown by the appearance of the processed p20 band (Fig. 4e and Supplementary Fig. 1). FISNA domain mutants R147E, E152R, N155A, R157E, K166E and E176R, and HD1 and WHD mutants Q424A and Q509A, were strongly defective in caspase-1 processing. FISNA mutant D213R and NBD mutants Q359A and H364E were less or not impaired in caspase-1 processing (Fig. 4e). These data confirmed the functional role of the structurally observed interface in the NLRP3 inflammasome disc.

Discussion

The cryo-EM structures of the NLRP3–NEK7–ASC complex presented here provide structural characterization of the active NLRP3 inflammasome, and show important implications in the mechanism of NLRP3 activation and new ways to target NLRP3. First, from these NLRP3 structures we identified the mechanism of NLRP3 oligomerization in the active state. We found that the FISNA domain is a critical mediator of both NLRP3 conformational change and oligomerization, which is consistent with defective NLRP3 activation by our single-site, structure-guided mutations and with previously reported

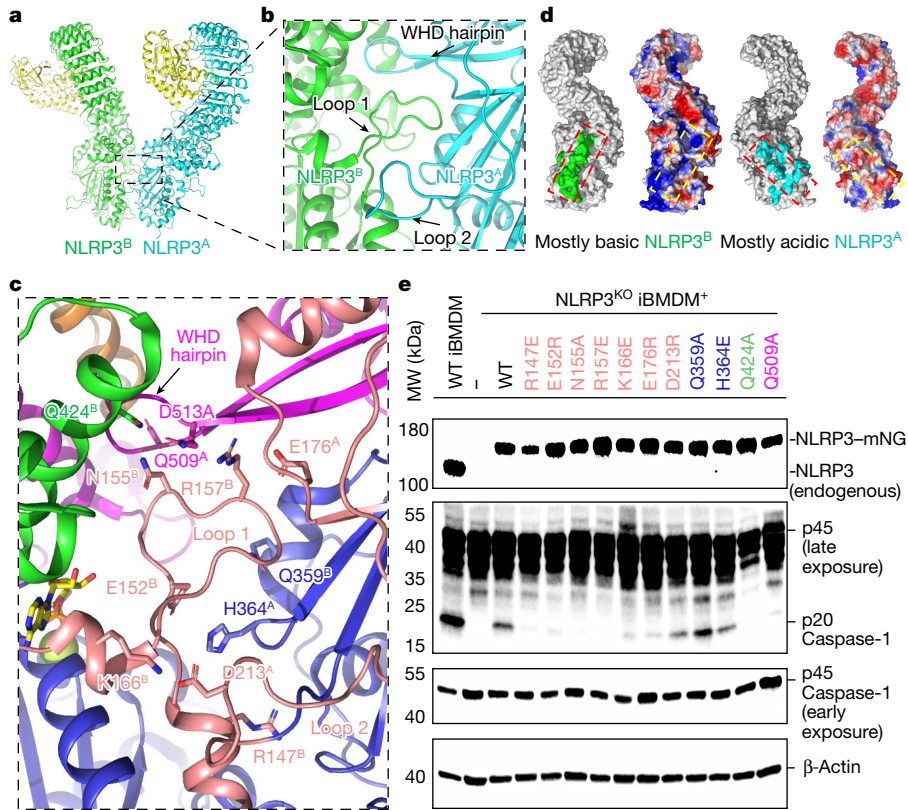


Fig. 4 | Interaction surfaces in the NLRP3 oligomer. **a**, Ribbon diagram of two neighbouring NLRP3–NEK7 subunits, shown with NLRP3^B in green and NLRP3^A in cyan. **b**, Close-up view of the interacting loops from two adjacent NLRP3 molecules. **c**, Interaction details for two neighbouring NLRP3 molecules. Ribbon diagrams and residues are coloured by domains. **d**, Mapped interactions at the NLRP3^B surface (green) and NLRP3^A surface (cyan), and their surface

electrostatic potentials. Dashed rectangles denote approximate locations of the surfaces. **e**, Caspase-1 processing by WT iBMDMs and NLRP3^{-/-} iBMDMs reconstituted with WT or mutant NLRP3 following LPS priming and nigericin treatment. These experiments were repeated twice. KO, knockout; mNG, mNeonGreen; MW, molecular weight.

impaired NLRP3 activation by complete or partial deletions of the FISNA domain¹³. The FISNA domain is absent in most NLRPs and much shortened in NLRC4 and NAIP5, indicating variable mechanisms in NLR oligomerization. This is despite the similar, though not identical, conformational change in NLRP3 in comparison with NLRC4. We further propose that NLRP3 conformational change requires both ATP (or dATP)⁹ binding and the FISNA domain, probably because of the insufficiency of either alone, to compensate for the energetic cost of activation, which echoes the conclusion that

both cytochrome c and dATP (or ATP) are required to fully activate the Apaf-1 apoptosome^{44,48}.

Second, the structures illuminate the role of LRR and NEK7 in NLRP3 inflammasome assembly. Surprisingly, we found that neither NEK7 nor LRR directly participates in NLRP3 oligomerization. What then are the functions of NEK7 and LRR? Together with the inactive cage structure of NLRP3 (refs. ^{9–11}), we propose that LRR and NEK7 are additional molecular switches in NLRP3 activation: whereas LRR is required for the inactive cage structure, its interaction with NEK7 at the MTOC

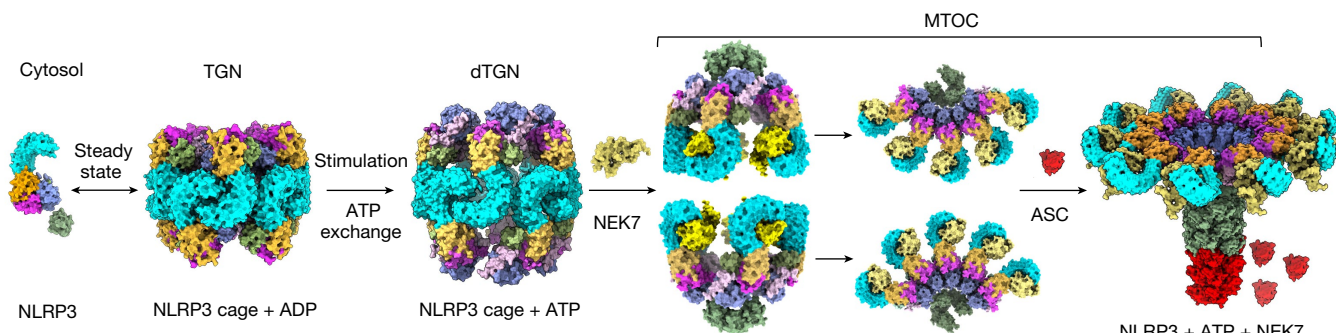


Fig. 5 | A structure-derived model of NLRP3 inflammasome activation. At a steady state after priming by TLR ligands such as LPS, upregulated NLRP3 is localized both in the cytosol and on the TGN in monomeric and cage forms, respectively. On stimulation, NLRP3 most probably undergoes conformational changes in the cage form and the TGN disperses into vesicles. These

NLRP3-containing vesicles are trafficked on microtubules to the MTOC, where the centrosome-localized protein NEK7 interacts with NLRP3 to open the cage into two halves, possibly leading to immediate rearrangement into active NLRP3 oligomers. Recruitment of ASC then helps to complete NLRP3 disc formation and transduce the activation signal. dTGN, dispersed TGN.

disrupts the cage to allow formation of the active NLRP3 disc. Thus the NLRP3 inflammasome pathway may comprise the following steps: (1) priming by TLR ligands such as LPS to upregulate NLRP3 expression and prepare cells in other ways; (2) formation of NLRP3 cage on the TGN before stimulation; (3) NLRP3 conformational change and TGN dispersion following nigericin stimulation; (4) trafficking of dispersed TGN vesicles on microtubules to the MTOC; (5) opening of NLRP3 cage by the centrosome-resident protein NEK7 into two halves already tethered together, even if weakly, by a short PYD filament⁹; and (6) formation of the NLRP3 disc in the active conformation assisted by, and capable of, ASC recruitment (Fig. 5). Although we do not have direct evidence, the last step in the pathway may utilize the two half-cages generated on NEK7 binding, each comprising five subunits in the case of human NLRP3 (ref. ¹⁰), to rearrange into an inflammasome disc. Thus, the unique NLRP3 pathway makes use of the already oligomeric cage to unfurl and convert into the active disc assembly, akin to a closed bud opening into a blooming flower.

Our active NLRP3 structures showed that NEK7 does not directly participate in NLRP3 oligomerization. In addition, unlike Apaf-1 or NAIP in which cytochrome c or flagellin binding overcomes autoinhibition^{41,42,44}, NEK7 binding is compatible with either inactive or active NLRP3 conformation and is thus unlikely to trigger NLRP3 activation. These observations help to rationalize how NLRP3 may be activated without NEK7 under certain conditions⁴⁹; we hypothesize that these conditions may associate with higher NLRP3 expression or destabilization of the cage, to enable the inflammasome assembly from either caged or monomeric NLRP3 (Extended Data Fig. 9a). Our structures also suggest how LRR-deleted NLRP3, which cannot form the cage, may form an active inflammasome when overexpressed⁵⁰, probably also in an NEK7-independent manner (Extended Data Fig. 9b). More studies are required to dissect how NLRP3 senses multiple stimuli, and to explain other mechanistic details of the NLRP3 pathway to guide therapeutic intervention.

Online content

Any methods, additional references, Nature Portfolio reporting summaries, source data, extended data, supplementary information, acknowledgements, peer review information; details of author contributions and competing interests; and statements of data and code availability are available at <https://doi.org/10.1038/s41586-022-05570-8>.

1. Wang, L., Sharif, H., Vora, S. M., Zheng, Y. & Wu, H. Structures and functions of the inflammasome engine. *J. Allergy Clin. Immunol.* **147**, 2021–2029 (2021).
2. Swanson, K. V., Deng, M. & Ting, J. P.-Y. The NLRP3 inflammasome: molecular activation and regulation to therapeutics. *Nat. Rev. Immunol.* **19**, 477–489 (2019).
3. Gaidt, M. M. & Hornung, V. The NLRP3 inflammasome renders cell death pro-inflammatory. *J. Mol. Biol.* **430**, 133–141 (2018).
4. Nozaki, K., Li, L. & Miao, E. A. Innate sensors trigger regulated cell death to combat intracellular infection. *Annu. Rev. Immunol.* **40**, 469–498 (2022).
5. Deets, K. A. & Vance, R. E. Inflammasomes and adaptive immune responses. *Nat. Immunol.* **22**, 412–422 (2021).
6. Coll, R. C. et al. MCC950 directly targets the NLRP3 ATP-hydrolysis motif for inflammasome inhibition. *Nat. Chem. Biol.* **15**, 556–559 (2019).
7. Tapia-Abellán, A. et al. MCC950 closes the active conformation of NLRP3 to an inactive state. *Nat. Chem. Biol.* **15**, 560–564 (2019).
8. Sharif, H. et al. Structural mechanism for NEK7-licensed activation of NLRP3 inflammasome. *Nature* **570**, 338–343 (2019).
9. Andreeva, L. et al. NLRP3 cages revealed by full-length mouse NLRP3 structure control pathway activation. *Cell* **184**, 6299–6312.e22 (2021).
10. Hochheiser, I. V. et al. Structure of the NLRP3 decamer bound to the cytokine release inhibitor CRID3. *Nature* **604**, 184–189 (2022).
11. Ohto, U. et al. Structural basis for the oligomerization-mediated regulation of NLRP3 inflammasome activation. *Proc. Natl. Acad. Sci. USA* **119**, e2121353119 (2022).
12. Dekker, C. et al. Crystal structure of NLRP3 NACHT domain with an inhibitor defines mechanism of inflammasome inhibition. *J. Mol. Biol.* **433**, 167309 (2021).
13. Tapia-Abellán, A. et al. Sensing low intracellular potassium by NLRP3 results in a stable open structure that promotes inflammasome activation. *Sci. Adv.* **7**, eabf4468 (2021).
14. Muñoz-Planillo, R. et al. K⁺ efflux is the common trigger of NLRP3 inflammasome activation by bacterial toxins and particulate matter. *Immunity* **38**, 1142–1153 (2013).
15. Magupalli, V. G. et al. HDAC6 mediates an aggresome-like mechanism for NLRP3 and pyrin inflammasome activation. *Science* **369**, eaas8995 (2020).
16. Chen, J. & Chen, Z. J. PtdIns4P on dispersed trans-Golgi network mediates NLRP3 inflammasome activation. *Nature* **564**, 71–76 (2018).
17. Li, X. et al. MARK4 regulates NLRP3 positioning and inflammasome activation through a microtubule-dependent mechanism. *Nat. Commun.* **8**, 15986 (2017).
18. Lu, A. et al. Unified polymerization mechanism for the assembly of ASC-dependent inflammasomes. *Cell* **156**, 1193–1206 (2014).
19. Hochheiser, I. V. et al. Directionality of PYD filament growth determined by the transition of NLRP3 nucleation seeds to ASC elongation. *Sci. Adv.* **8**, eabn7583 (2022).
20. Li, Y. et al. Cryo-EM structures of ASC and NLRC4 CARD filaments reveal a unified mechanism of nucleation and activation of caspase-1. *Proc. Natl. Acad. Sci. USA* **115**, 10845–10852 (2018).
21. Lu, A. et al. Molecular basis of caspase-1 polymerization and its inhibition by a new capping mechanism. *Nat. Struct. Mol. Biol.* **23**, 416–425 (2016).
22. He, Y., Zeng, M. Y., Yang, D., Motro, B. & Núñez, G. NEK7 is an essential mediator of NLRP3 activation downstream of potassium efflux. *Nature* **530**, 354–357 (2016).
23. Schmid-Burgk, J. L. et al. A genome-wide CRISPR (clustered regularly interspaced short palindromic repeats) screen identifies NEK7 as an essential component of NLRP3 inflammasome activation. *J. Biol. Chem.* **291**, 103–109 (2016).
24. Shi, H. et al. NLRP3 activation and mitosis are mutually exclusive events coordinated by NEK7, a new inflammasome component. *Nat. Immunol.* **17**, 250–258 (2016).
25. Martinon, F., Burns, K. & Tschopp, J. The inflammasome: a molecular platform triggering activation of inflammatory caspases and processing of proIL-β. *Mol. Cell* **10**, 417–426 (2002).
26. Ding, J. et al. Pore-forming activity and structural autoinhibition of the gasdermin family. *Nature* **535**, 111–116 (2016).
27. Liu, X. et al. Inflammasome-activated gasdermin D causes pyroptosis by forming membrane pores. *Nature* **535**, 153–158 (2016).
28. He, W.-t. et al. Gasdermin D is an executor of pyroptosis and required for interleukin-1β secretion. *Cell Res.* **25**, 1285–1298 (2015).
29. Kayagaki, N. et al. Caspase-11 cleaves gasdermin D for non-canonical inflammasome signalling. *Nature* **526**, 666–671 (2015).
30. Shi, J. et al. Cleavage of GSDMD by inflammatory caspases determines pyroptotic cell death. *Nature* **526**, 660–665 (2015).
31. Lieberman, J., Wu, H. & Kagan, J. C. Gasdermin D activity in inflammation and host defense. *Sci. Immunol.* **4**, eaav1447 (2019).
32. Gaidt, M. M. & Hornung, V. Pore formation by GSDMD is the effector mechanism of pyroptosis. *EMBO J.* **35**, 2167–2169 (2016).
33. Booshehri, L. M. & Hoffman, H. M. Caps and NLRP3. *J. Clin. Immunol.* **39**, 277–286 (2019).
34. Touitou, I. et al. Infevers: an evolving mutation database for auto-inflammatory syndromes. *Hum. Mutat.* **24**, 194–198 (2004).
35. Mangan, M. S. et al. Targeting the NLRP3 inflammasome in inflammatory diseases. *Nat. Rev. Drug Discov.* **17**, 588–606 (2018).
36. Duncan, J. A. et al. Cryopyrin/NALP3 binds ATP/dATP, is an ATPase, and requires ATP binding to mediate inflammatory signaling. *Proc. Natl. Acad. Sci. USA* **104**, 8041–8046 (2007).
37. Richards, M. W. et al. An autoinhibitory tyrosine motif in the cell-cycle-regulated Nek7 kinase is released through binding of Nek9. *Mol. Cell* **36**, 560–570 (2009).
38. Zhang, L. et al. Cryo-EM structure of the activated NAIP2-NLRC4 inflammasome reveals nucleated polymerization. *Science* **350**, 404–409 (2015).
39. Hu, Z. et al. Structural and biochemical basis for induced self-propagation of NLRC4. *Science* **350**, 399–404 (2015).
40. Hu, Z. et al. Crystal structure of NLRC4 reveals its autoinhibition mechanism. *Science* **341**, 172–175 (2013).
41. Tenthorey, J. L. et al. The structural basis of flagellin detection by NAIP5: a strategy to limit pathogen immune evasion. *Science* **358**, 888–893 (2017).
42. Yang, X. et al. Structural basis for specific flagellin recognition by the NLR protein NAIP5. *Cell Res.* **28**, 35–47 (2018).
43. Sandall, C. F., Ziehr, B. K. & MacDonald, J. A. ATP-binding and hydrolysis in inflammasome activation. *Molecules* **25**, 4572 (2020).
44. Zhou, M. et al. Atomic structure of the apoptosome: mechanism of cytochrome c-and dATP-mediated activation of Apaf-1. *Genes Dev.* **29**, 2349–2361 (2015).
45. Yan, N. et al. Structure of the CED-4-CED-9 complex provides insights into programmed cell death in *Caenorhabditis elegans*. *Nature* **437**, 831–837 (2005).
46. Qi, S. et al. Crystal structure of the *Caenorhabditis elegans* apoptosome reveals an octameric assembly of CED-4. *Cell* **141**, 446–457 (2010).
47. Krissinel, E. & Henrick, K. Inference of macromolecular assemblies from crystalline state. *J. Mol. Biol.* **372**, 774–797 (2007).
48. Li, P. et al. Cytochrome c and dATP-dependent formation of Apaf-1/caspase-9 complex initiates an apoptotic protease cascade. *Cell* **91**, 479–489 (1997).
49. Schmacke, N. A. et al. IKK β primes inflammasome formation by recruiting NLRP3 to the trans-Golgi network. *Immunity* <https://doi.org/10.1016/j.immuni.2022.10.021> (2022).
50. Hafner-Bratković, I. et al. NLRP3 lacking the leucine-rich repeat domain can be fully activated via the canonical inflammasome pathway. *Nat. Commun.* **9**, 5182 (2018).

Publisher's note Springer Nature remains neutral with regard to jurisdictional claims in published maps and institutional affiliations.

Springer Nature or its licensor (e.g. a society or other partner) holds exclusive rights to this article under a publishing agreement with the author(s) or other rightsholder(s); author self-archiving of the accepted manuscript version of this article is solely governed by the terms of such publishing agreement and applicable law.

© The Author(s), under exclusive licence to Springer Nature Limited 2022

Methods

Plasmid construction

Full-length human NLRP3 and full-length human NEK7 were cloned into pTT3 vector with an N-terminal MBP tag and into pFLAG-CMV4 vector with an N-terminal FLAG tag, respectively. Human ASC^{PYD} (residues 1–106) was cloned into pDB-His-MBP vector and expressed as an MBP fusion protein with an additional N-terminal 6× His tag as reported previously¹⁸. For reconstitution of WT and mutant NLRP3 into NLRP3^{−/−} mouse bone marrow-derived macrophages (BMDMs), full-length human NLRP3 was cloned into an in-house-modified pLV-eGFP vector in which enhanced green fluorescent protein was replaced by mNG, as reported previously⁸. All constructs were confirmed by sequencing.

Protein expression and purification

Expi293F cells, maintained in 800 ml of Expi293 Expression Media (ThermoFisher), were fed with 6 mM KCl and grown to 2.0×10^6 cells ml^{−1}. These were transiently cotransfected with 0.5 mg of NLRP3 plasmid and 0.3 mg of NEK7 plasmid using 2.4 mg of polyethylenimine (Polysciences, Inc.). Cells were fed with 10 mM sodium butyrate and 8 ml of 45% D-(+)-glucose solution at 12 h after transfection. Cells were harvested another 48 h later by 20 min centrifugation at 2,500 rpm. The collected cells were resuspended in PBS, treated for 30 min with 20 μM z-VAD-FMK, a pan-caspase inhibitor, and stimulated for a further 30 min with 10 μg ml^{−1} nigericin (13.4 μM). After stimulation, cells were lysed by sonication in the presence of a protease inhibitor cocktail (Roche) and centrifuged at 40,000 rpm for 1 h. The supernatant was collected and incubated with anti-FLAG resin for 1 h at 4 °C, with gentle rotation, and the resin washed with PBS. Bound proteins were eluted using PBS with the addition of 0.1 mg ml^{−1} FLAG peptide, and concentrated. His-MBP-ASC^{PYD} was expressed in *Escherichia coli* and purified by Ni-NTA affinity and gel filtration chromatography using a Superdex 200 column. To reconstitute the active NLRP3 inflammasome, 1 mM ATPγS, 2.5 mM MgCl₂ and either one- or tenfold molar excess ASC^{PYD} were added to the NLRP3–NEK7 complex, and MBP tags on NLRP3 and ASC^{PYD} were removed by incubation overnight with tobacco etch virus protease at 1:20 molar ratio. The molar concentration of ASC or the NLRP3–NEK7 complex was determined by optical density (OD₂₈₀) absorption, extinction coefficient and the molecular weight of His-MBP-ASC or the MBP–NLRP3–NEK7 complex. The mixture was applied to a Superose 6 gel filtration column equilibrated with running buffer (20 mM Tris pH 8.0, 150 mM NaCl and 1 mM tris(2-carboxyethyl)phosphine hydrochloride), and the peak near void was collected and concentrated to 0.8 mg ml^{−1} for EM experiments.

Negative-staining electron microscopy

Five microlitres of tenfold diluted NLRP3–NEK7–ASC complex was applied to a copper grid (Electron Microscopy Sciences, no. FCF400CU50), incubated for 1 min and absorbed with filter paper. The grid was then stained with 2% uranyl formate for 1 min and air-dried. Images were collected using a Tecnai G2 Spirit BioTWIN transmission electron microscope.

Cryo-EM grid preparation and data acquisition

Before grid preparation, 1 mM ATPγS and 2.5 mM MgCl₂ were added to the protein sample with incubation on ice for 1 h. A 3.5 μl drop containing the NLRP3–NEK7–ASC complex was loaded onto a glow-discharged Quantifoil grid (R1.2/1.3 400-mesh gold-supported holey carbon, Electron Microscopy Sciences), blotted for 3–4 s under 100% humidity at 4 °C and plunged into liquid ethane with Mark IV Vitrobot (ThermoFisher). Automated data collection was performed using SerialEM (Mastronarde, 2005), and videos were acquired on a Titan Krios microscope (ThermoFisher) operating at 300 keV and equipped with a BioQuantum K3 Imaging Filter (Gatan, slit width 20 eV). Videos

were recorded with a K3 Summit direct electron detector (Gatan) operating in super-resolution mode at $\times 81,000$ magnification (0.53 Å per pixel). All videos were exposed at a total dose of 50.4 e Å^{−2} over 40 frames with defocus range between −1.0 and −2.0 μm.

Cryo-EM data processing

All data-processing software support was acquired from the SGBGrid Consortium. Overall, 11,356 videos were corrected by beam-induced motion using the Relion v.3.1 (ref. ⁵¹) implementation of the MotionCor2 algorithm⁵². The contrast transfer function (CTF) and defocus estimation of micrographs were calculated by CTFFIND4 (ref. ⁵³). Images were imported into CryoSPARC⁵⁴ for further data processing. Two hundred images were selected and autopicked using the Blob Picker function in CryoSPARC, resulting in 95,296 particles. 2D classification was then used to generate templates for the Template Picker function in CryoSPARC, from which a total of 808,941 particles were picked. All particles were extracted with 8× binning (4.24 Å pixel size) at a box size of 128 pixels, then subjected to reference-free 2D classification. Bad particles were rejected, and good 2D classes with clear top or side views were selected. After rounds of 2D classification, 322,527 particles were selected and extracted with 2× binning at a box size of 512 pixels. The resulting particles were applied for ab initio reconstruction with $K = 5$, followed by heterogeneous refinement. Further reference-free 2D classification of particles from the two best three-dimensional classes was performed, resulting in three final datasets corresponding to 140,634 incomplete discs with four blades, 51,576 10-fold discs and 31,004 11-fold discs. Ab initio reconstruction and homogeneous refinement were conducted for each dataset without applying symmetry, which resulted in a 4.38 Å map for the tenfold disc and a 5.12 Å map for the 11-fold disc; for incomplete discs nonuniform refinement was further performed, resulting in a 3.82 Å map. For the 10- and 11-fold discs, C10 and C11 symmetry were applied during nonuniform refinement, leading to 3.49 and 3.89 Å maps, respectively. After local CTF refinement and local masked refinement, maps for the 10- and 11-fold discs were improved to 3.40 and 3.79 Å resolution, respectively.

PYD filament reconstruction

We selected 43,255 particles containing stacked discs with short filaments in the middle from the initial 2D classification and re-extracted with 2× binning at a box size of 200 pixels. After further 2D classification, 33,227 particles were selected for ab initio reconstruction without helical symmetry, and then for helical reconstruction starting from the helical parameter in previously solved PYD filament structures^{18,55} (C3 symmetry, 54° in twist and 14 Å in rise per subunit). Two rounds of helical refinement converged at refined twist of 54.926° and rise of 14.320 Å, resulting in a 3.3 Å map of the NLRP3 PYD filament.

Model building and structure representation

The cryo-EM maps were first fit with the NLRP3–NEK7 complex structure⁸ (PDB: 6NPY), NEK7 structure³⁷ (2WQM) and an AlphaFold predicted model⁵⁶ using UCSF Chimera⁵⁷ or ChimeraX⁵⁸, followed by manual adjustment in Coot⁵⁹ and real-space refinement in Phenix⁶⁰. For all structures we used PISA5 (ref. ⁴⁷) to analyse interactions. Structure representations were generated in ChimeraX⁵⁸ and Pymol⁶¹.

Generation of stable cell lines

We used lentiviruses to reconstitute NLRP3^{−/−} mouse iBMDMs with WT or mutant full-length mNG-tagged human NLRP3 following a previously described protocol⁸, with the following modification. After spinfection to infect NLRP3^{−/−} mouse iBMDMs with lentiviruses, cells were incubated for the expression of reconstituted proteins for 48 h and sorted on either a BD FACSAria Fusion or a FACSAria II cell sorter using a 100 μm nozzle at 20 psi. Sorted populations were gated to exclude dead and nonfluorescent cells.

Immunoblotting of whole-cell lysates

Wild-type iBMDMs, NLRP3^{-/-} iBMDMs and NLRP3^{-/-} iBMDMs reconstituted with mNG-tagged NLRP3 WT and mutants were seeded at 1×10^6 cells per well on a six-well tissue culture plate. The following day, cells were treated with 1 $\mu\text{g ml}^{-1}$ LPS (Invivogen, no. tIrl-b5lps) for 4 h followed by NLRP3 activation with 20 μM nigericin (Sigma-Aldrich, no. N7143-5MG) for 1 h. Medium was discarded and the whole-cell lysate was prepared by the addition of 100 μl lysis buffer (150 mM NaCl, 50 mM Tris-HCl pH 7.5, 1% NP-40 and 5% glycerol) to each well. After 30 min, lysates were centrifuged for 10 min at 15,000 rpm to remove the pellets and SDS sample buffer was added, followed by loading onto a 4–12% Bis-Tris PAGE gel (Invitrogen, no. NP0336BOX) along with a Page Ruler Preset Ladder (Thermo Scientific, no. 26616). NLRP3, β -actin and the cleaved caspase-1 p20 fragment were visualized by immunoblotting using mouse primary antibodies anti-NLRP3 (1:2,000; Adipogen, no. AG-20B-0014-C100), mouse anti- β -actin (1:2,000; Sigma-Aldrich, no. A2228-100UL) and rabbit anti-p20 of caspase-1 (1:1,000; Cell Signaling, no. 89332S), respectively. Secondary antibodies used were anti-mouse-HRP (1:5,000; Cell Signaling, no. 7076S) and anti-rabbit-HRP (1:2,500; Cell Signaling, no. 7074S).

Reporting summary

Further information on research design is available in the Nature Portfolio Reporting Summary linked to this article.

Data availability

Atomic coordinates of the tenfold NLRP3–NEK7 assembly structure and NLRP3 PYD filament have been deposited in PDB under accession nos. 8EJ4 and 8ERT, respectively. Corresponding cryo-EM density maps have been deposited in the Electron Microscopy Data Bank under accession nos. EMD-28175 and EMD-28560, respectively. All other data are available from the corresponding authors on reasonable request.

51. Zivanov, J. et al. New tools for automated high-resolution cryo-EM structure determination in RELION-3. *eLife* **7**, e42166 (2018).

52. Zheng, S. Q. et al. MotionCor2: anisotropic correction of beam-induced motion for improved cryo-electron microscopy. *Nat. Methods* **14**, 331–332 (2017).
53. Rohou, A. & Grigorieff, N. CTFFIND4: fast and accurate defocus estimation from electron micrographs. *J. Struct. Biol.* **192**, 216–221 (2015).
54. Punjani, A., Rubinstein, J. L., Fleet, D. J. & Brubaker, M. A. cryoSPARC: algorithms for rapid unsupervised cryo-EM structure determination. *Nat. Methods* **14**, 290–296 (2017).
55. Shen, C. et al. Molecular mechanism for NLRP6 inflammasome assembly and activation. *Proc. Natl Acad. Sci. USA* **116**, 2052–2057 (2019).
56. Tunyasuvunakool, K. et al. Highly accurate protein structure prediction for the human proteome. *Nature* **596**, 590–596 (2021).
57. Goddard, T. D., Huang, C. C. & Ferrin, T. E. Visualizing density maps with UCSF Chimera. *J. Struct. Biol.* **157**, 281–287 (2007).
58. Goddard, T. D. et al. UCSF ChimeraX: meeting modern challenges in visualization and analysis. *Protein Sci.* **27**, 14–25 (2018).
59. Emsley, P., Lohkamp, B., Scott, W. G. & Cowtan, K. Features and development of Coot. *Acta Crystallogr. D Biol. Crystallogr.* **66**, 486–501 (2010).
60. Adams, P. D. et al. PHENIX: a comprehensive Python-based system for macromolecular structure solution. *Acta Crystallogr. D Biol. Crystallogr.* **66**, 213–221 (2010).
61. DeLano, W. L. Pymol: an open-source molecular graphics tool. *CCP4 Newslett. Protein Crystallogr.* **40**, 82–92 (2002).

Acknowledgements We thank H. Sharif, L. Andreeva, M. Mohammad, L. Wang and L. David for earlier work on this project, and Wu laboratory members for useful discussions. We thank Z. Yang for making lentiviruses and reconstitution of NLRP3 mutants into NLRP3^{-/-} iBMDMs. For cryo-EM data collection we thank R. Walsh, S. Sterling, M. Megan, S. Rawson and Z. Li at the Harvard Cryo-EM Center for Structural Biology, and K. Song and J. Chang at the Cryo-EM Core Facility at University of Massachusetts Medical School. We thank K. Fitzgerald at University of Massachusetts Medical School for NLRP3^{-/-} iBMDMs. We also thank R. Tomaino and Taplin Biological Mass Spectrometry Facility for protein analysis. Our research used software and computing support at SBGrid. This work was supported by US National Institutes of Health (nos. R01AI124491 to H.W. and R21AR079766 to V.G.M.), a postdoctoral fellowship from the KidneyCure Foundation (to L.X.) and a Faculty Career Development Fellowship from OFD/BTREC/CTREC Program of Boston Children's Hospital (to V.G.M.).

Author contributions H.W. and L.X. conceived the study. V.G.M. generated and carried out initial expression of NLRP3 and NEK7 constructs by immunoblotting. L.X. designed and performed all experiments and H.W. supervised the project. L.X. and H.W. wrote the manuscript.

Competing interests H.W. is a cofounder of Ventus Therapeutics. L.X. and V.G.M. declare no competing interests.

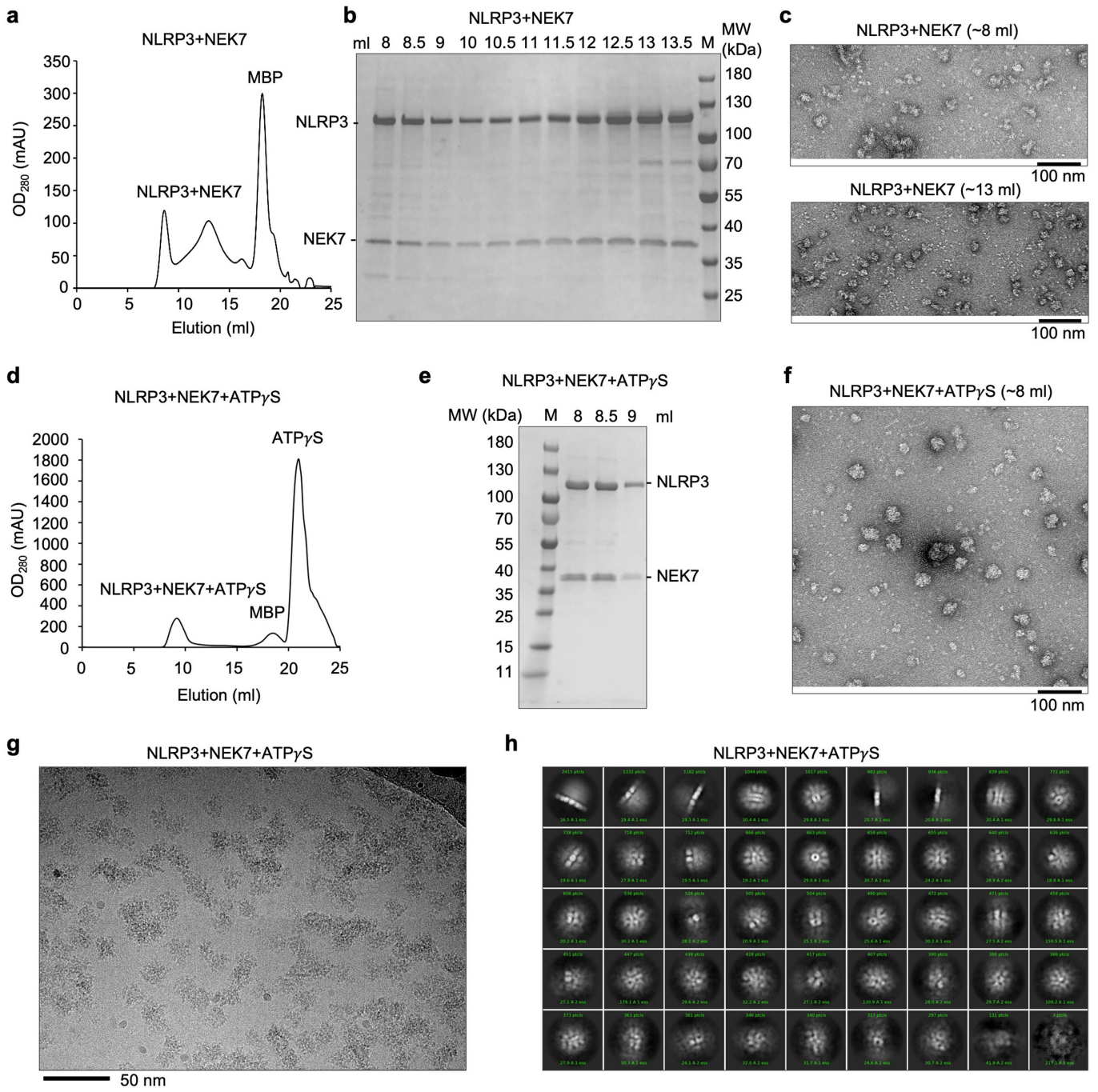
Additional information

Supplementary information The online version contains supplementary material available at <https://doi.org/10.1038/s41586-022-05570-8>.

Correspondence and requests for materials should be addressed to Hao Wu.

Peer review information *Nature* thanks Edward Miao and the other, anonymous, reviewer(s) for their contribution to the peer review of this work.

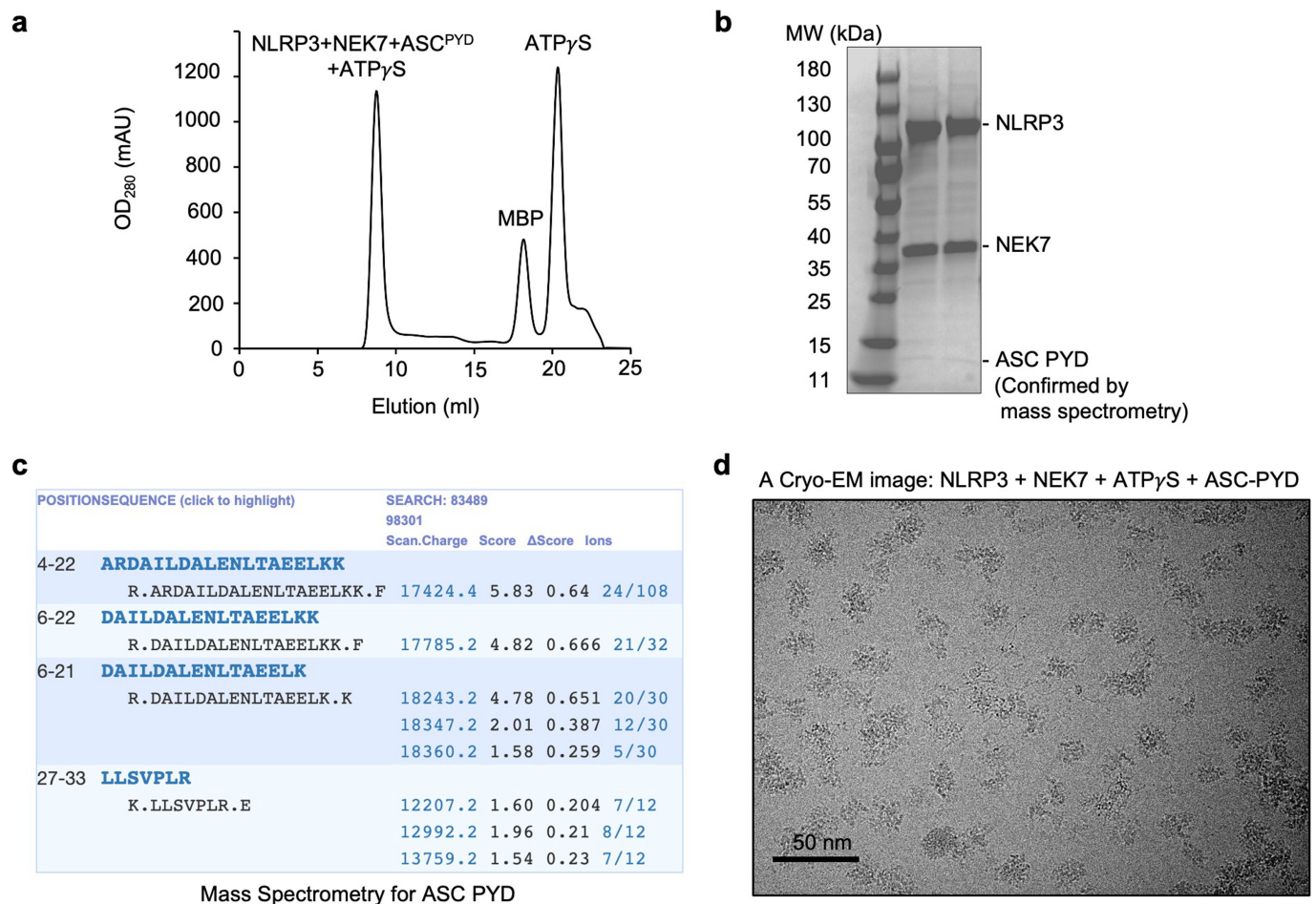
Reprints and permissions information is available at <http://www.nature.com/reprints>.



Extended Data Fig. 1 | Preparation and characterization of the NLRP3-NEK7 complex. **a**, Gel filtration profile of the NLRP3-NEK7 complex showing the two peaks. **b**, SDS-polyacrylamide gel electrophoresis (PAGE) of gel filtration fractions for the NLRP3-NEK7 complex. Locations of the two component proteins are labeled. **c**, Representative negative-staining images from the two NLRP3-NEK7 complex peaks. **d**, Gel filtration profile of the NLRP3-NEK7 complex with ATP γ S showing one major peak. **e**, SDS-PAGE of the gel filtration

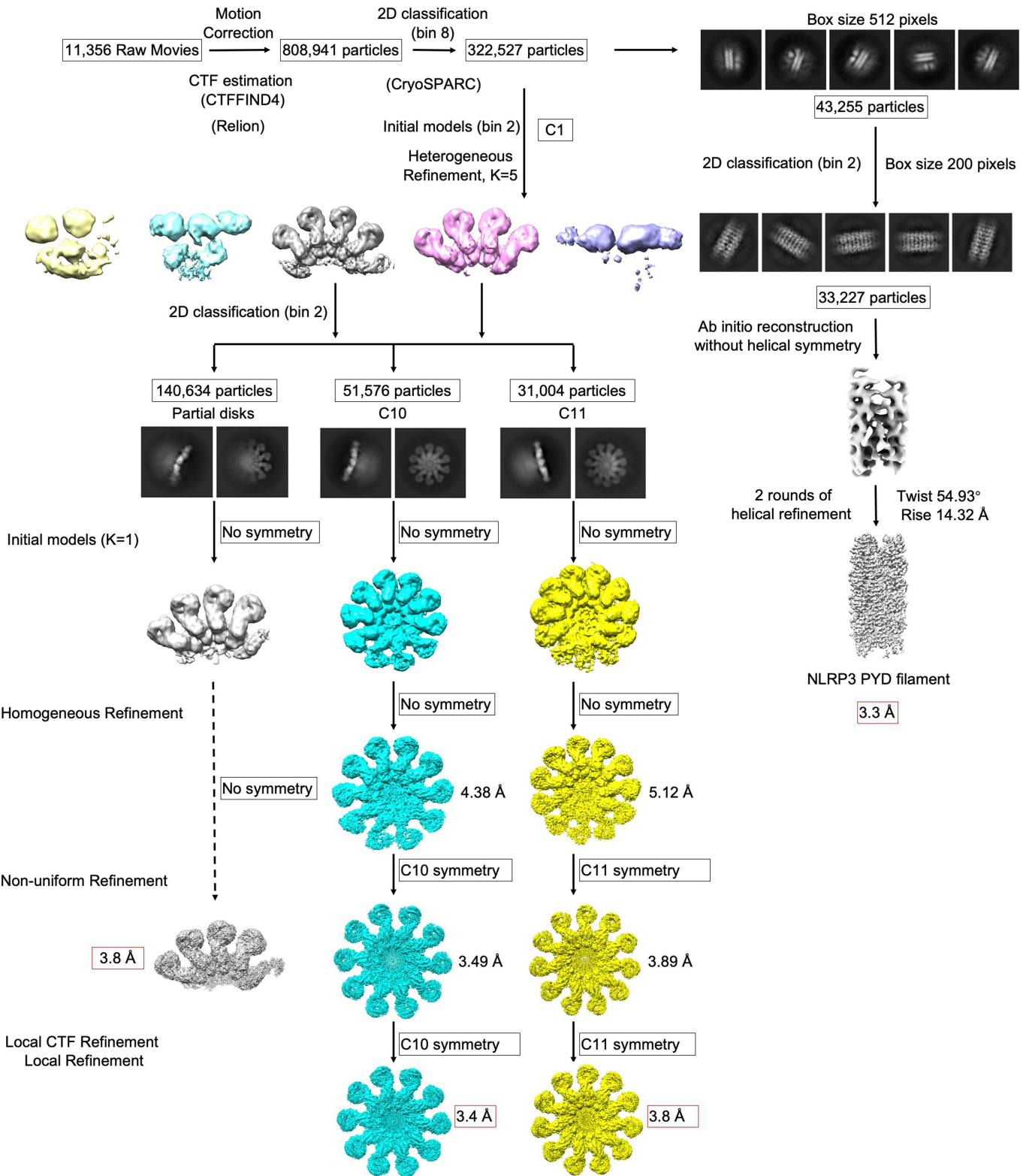
fractions for the NLRP3-NEK7 complex with ATP γ S. Locations of the two component proteins are labeled. **f**, A representative negative-staining image from the peak containing NLRP3, NEK7 and ATP γ S. **g**, A representative cryo-EM image from the peak containing NLRP3, NEK7 and ATP γ S. Experiments in (a-g) were repeated at least three times. **h**, 2D classes from cryo-EM images of the NLRP3-NEK7 complex with ATP γ S. No full disk was observed.

Article



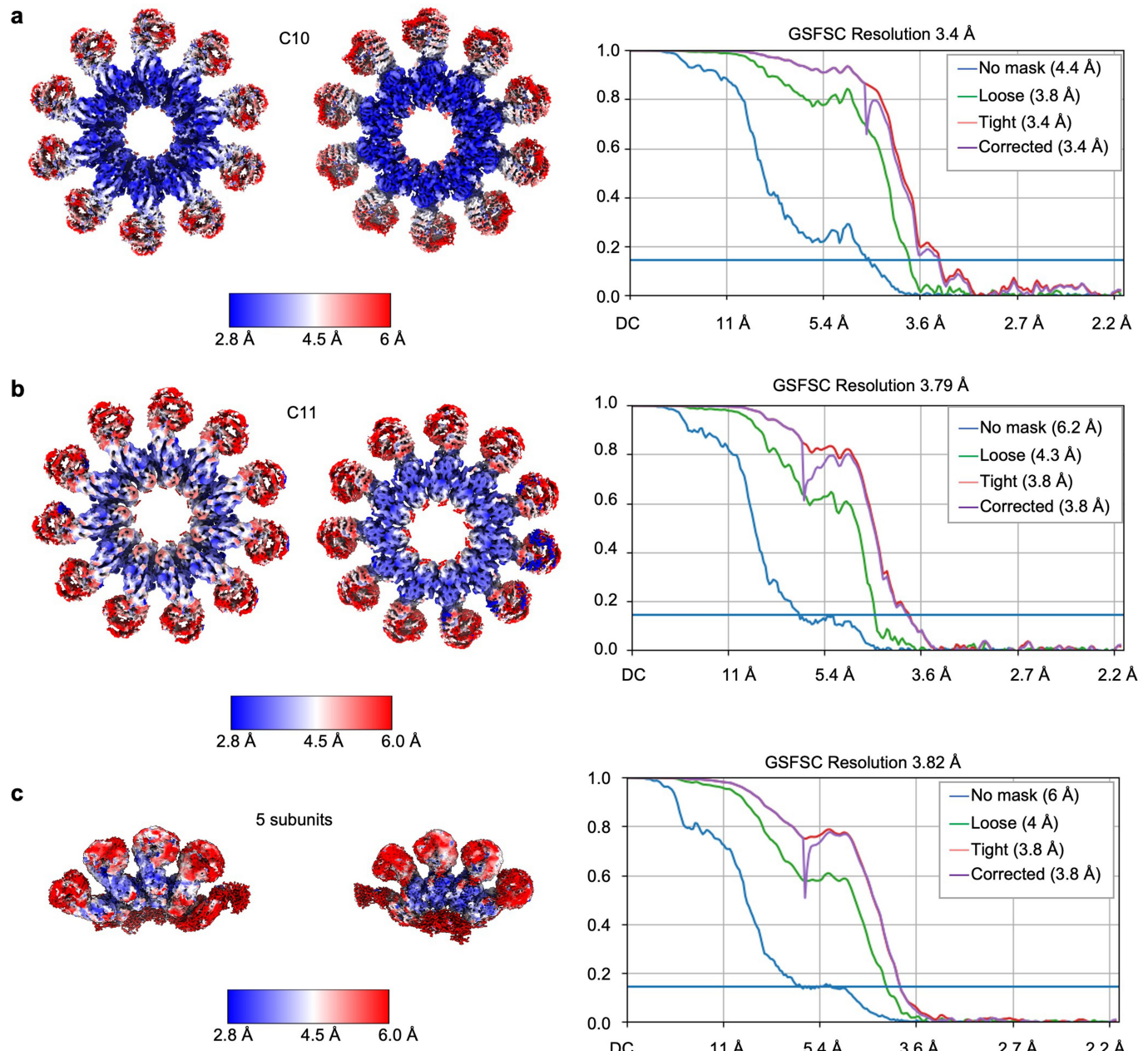
Extended Data Fig. 2 | Preparation and characterization of NLRP3-NEK7-ASC inflammasome complexes. **a**, Gel filtration profile of the NLRP3-NEK7-ASC complex. **b**, SDS-PAGE of the near void peak from the gel filtration chromatography. Locations of the three component proteins are labelled. **c**, Mass

spectrometry that detected ASC PYD in the band in (b). **d**, A representative cryo-EM image from a sample containing NLRP3, NEK7, ATP γ S, and 1:1 ASC PYD. Experiments in (a-b) and (d) were repeated at least three times.

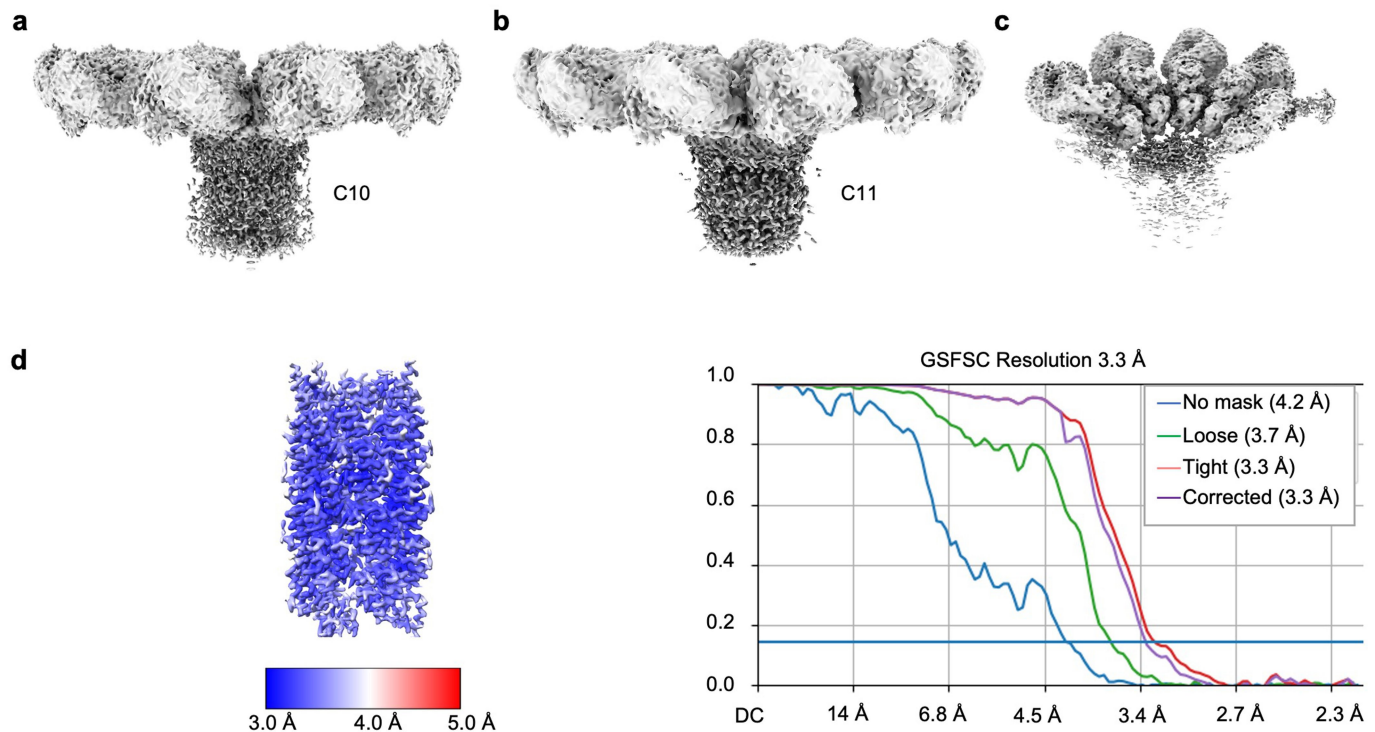


Extended Data Fig. 3 | Flow chart for cryo-EM data processing of the NLRP3-NEK7-ASC inflammasome complex. Data processing details can be found in Methods.

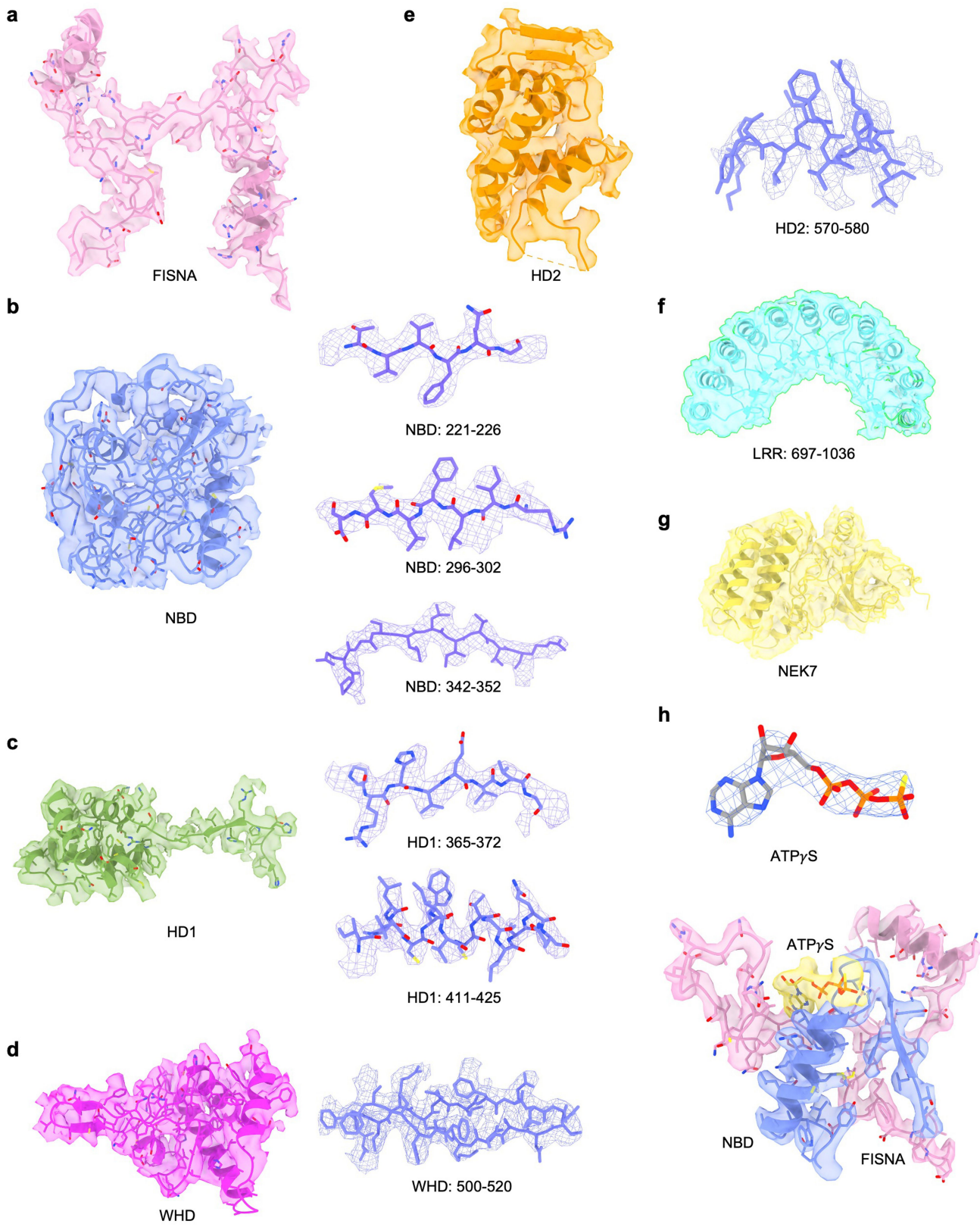
Article



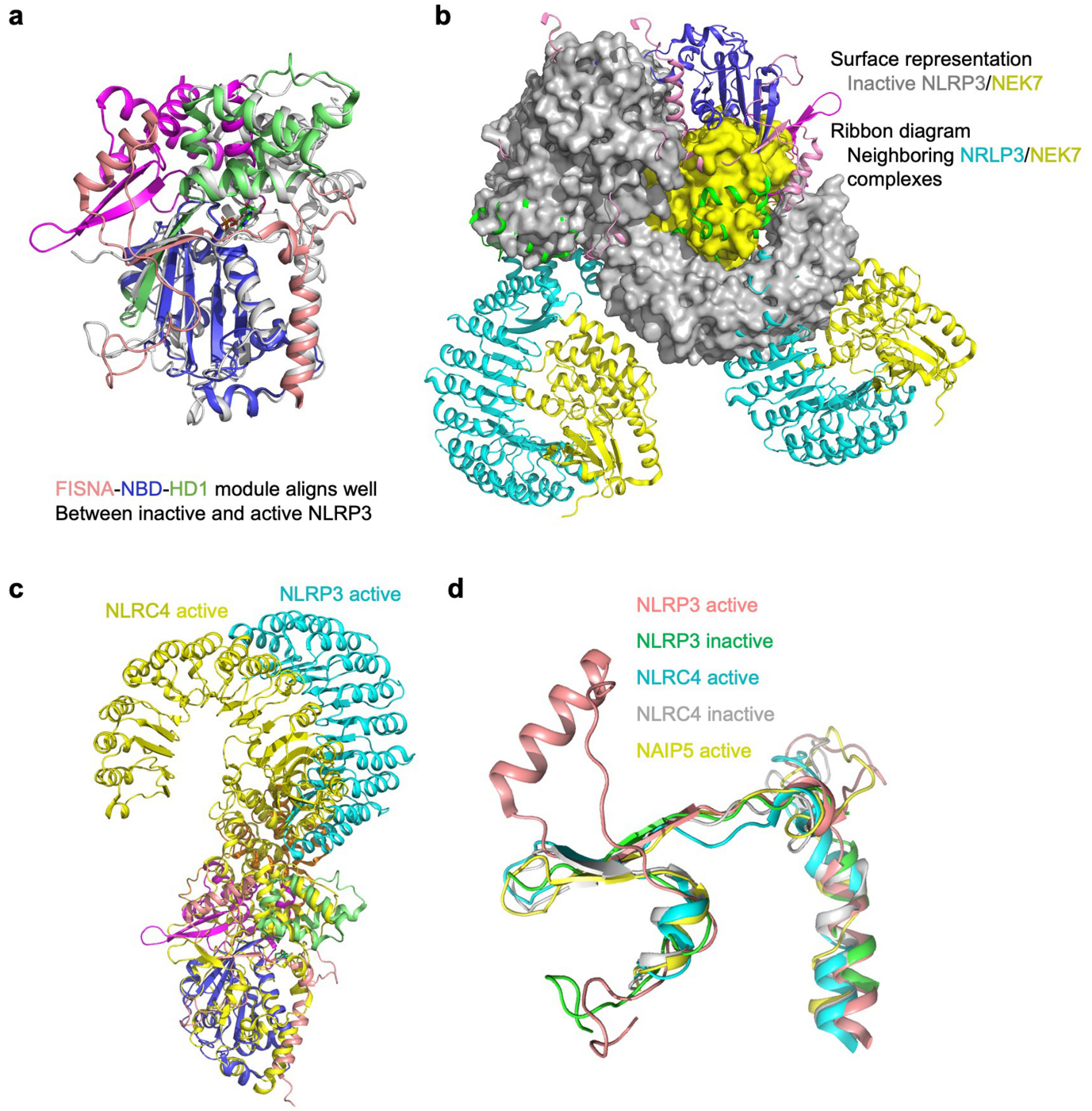
Extended Data Fig. 4 | Local resolution distributions and Fourier shell correlation (FSC) curves. a-c, The C10 NLRP3-NEK7-ASC complex (a), the C11 NLRP3-NEK7-ASC complex (b), and the partial NLRP3-NEK7 disk containing primarily 5 subunits (c).



Extended Data Fig. 5 | PYD helical filament. **a-c.** Side views of the cryo-EM maps of the C10 NLRP3-NEK7-ASC complex (a), the C11 NLRP3-NEK7-ASC complex (b) and the partial disk of the NLRP3-NEK7 complex (c). **d.** Local resolution distribution and Fourier shell correlation (FSC) curve of the NLRP3 PYD filament.



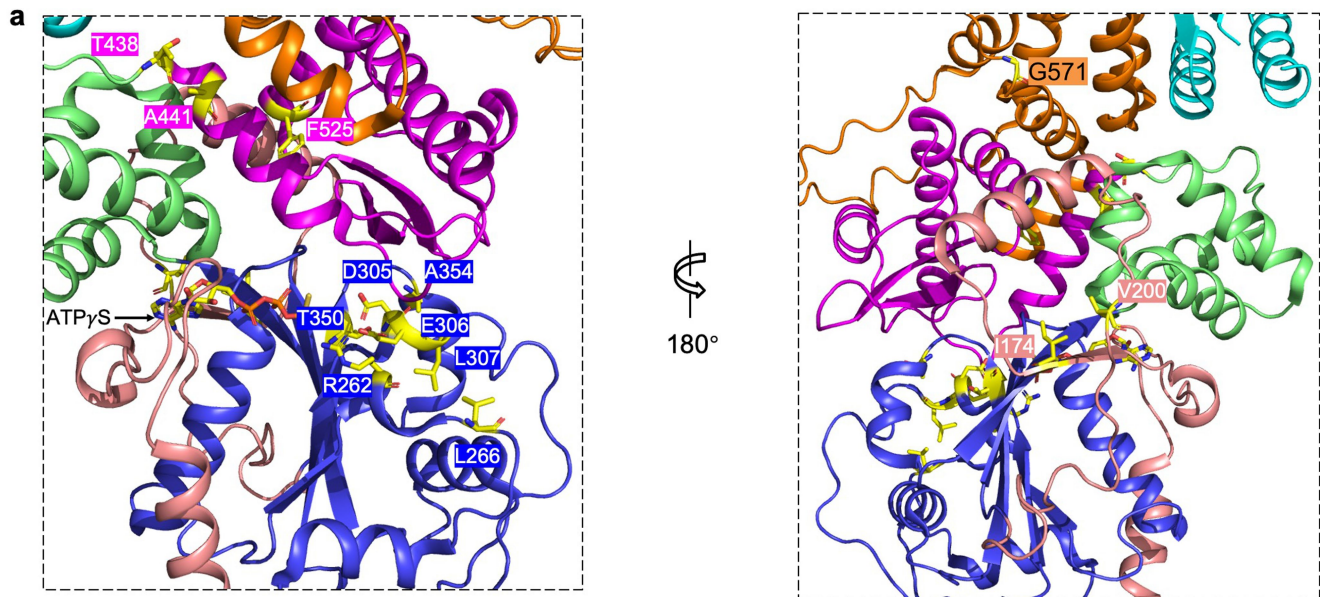
Extended Data Fig. 6 | Close-up evaluation of the C10 NLRP3-NEK7-ASC complex map quality. **a-h**, Cryo-EM maps in individual regions (labelled) superimposed with the final model.



Extended Data Fig. 7 | Conformational change and comparison with NLRC4.
a, Superposition of active NLRP3 (in domain colours) and inactive NLRP3 (PDB: 6NPY in grey) by the FISNA-NBD-HD1 domain. The WHD domain of inactive NLRP3 situates behind the superimposed HD1, different from that of active NLRP3. **b**, Superposition of active NLRP3 and inactive NLRP3 (PDB: 6NPY in grey), showing the LRR domain and NEK7 of the inactive NLRP3-NEK7 complex

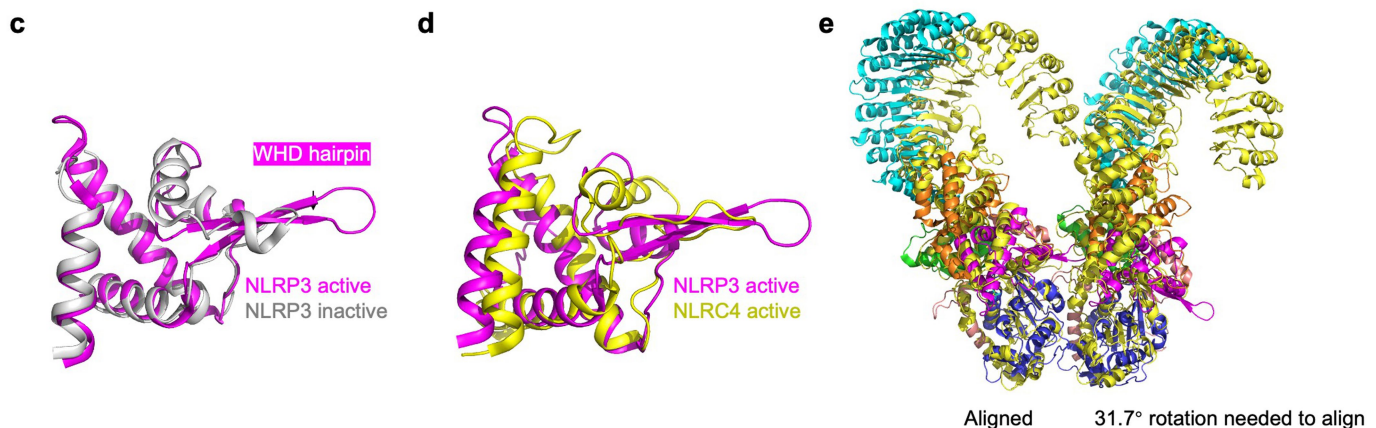
would have been in clash with a neighbouring NLRP3 molecule. **c**, Superposition of active NLRP3 with active NLRC4 (PDB: 3JBL in yellow) by the FISNA-NBD-HD1 domain. **d**, Superposition of the FISNA domain from active NLRP3 (salmon), inactive NLRP3 (PDB: 6NPY in green), active NLRC4 (PDB: 3JBL in cyan), inactive NLRC4 (PDB: 4KXF in grey), and active NAIP5 (6B5B in yellow).

Article



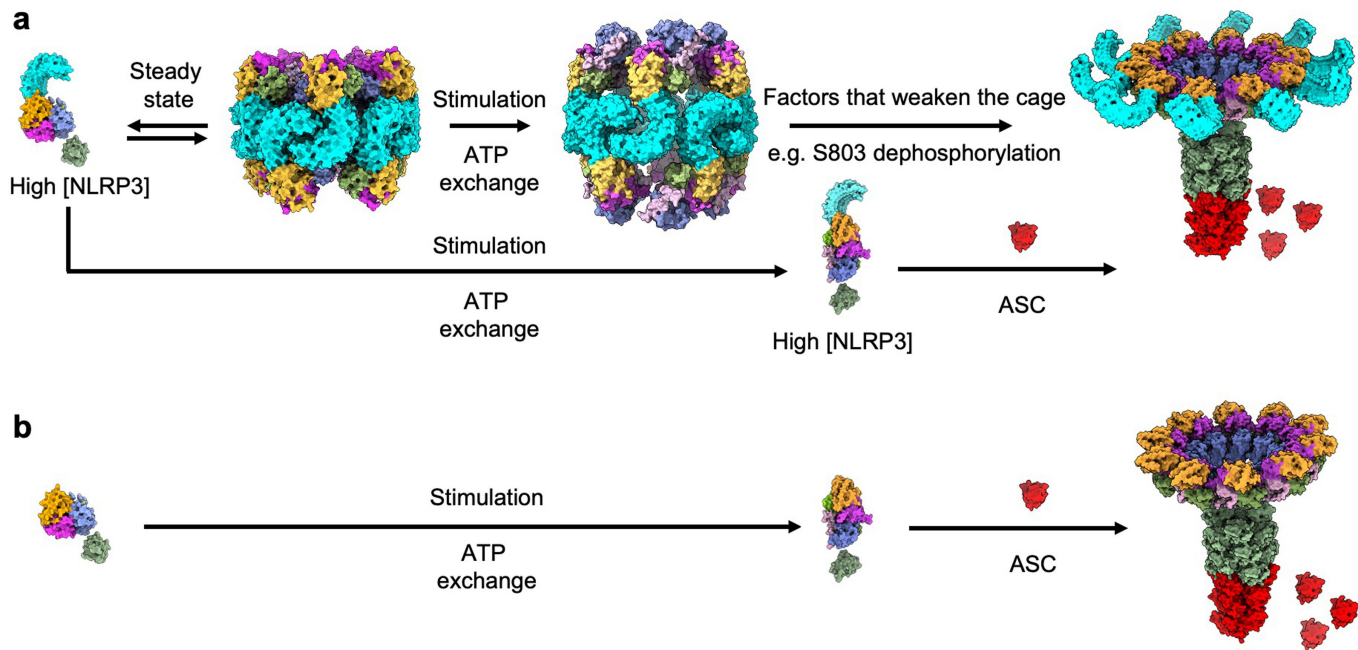
b

| Human NLRP3 | Mouse NLRP3 | Disease | Domain | Structural effect | PISA analysis |
|-------------|-------------|-----------------------|--------|------------------------------|------------------|
| I174T | V170 | CINCA/NOMID Syndrome | FISNA | NBD interaction | Buried |
| V200M | S196 | | FISNA | Local conformation | Exposed |
| R262W, L, P | R258 | Muckle-Wells Syndrome | NBD | Local conformation | Exposed |
| L266P | L262 | CINCA/NOMID Syndrome | NBD | Local conformation | Partially buried |
| D305N, G | D301 | CINCA/NOMID Syndrome | NBD | Local conformation– Walker B | Buried |
| E306K | E302 | CINCA/NOMID Syndrome | NBD | Local conformation– Walker B | Partially buried |
| L307P | L303 | | NBD | Local conformation | Buried |
| T350M | T346 | Muckle-Wells Syndrome | NBD | Local conformation | Buried |
| A354V | A350 | Muckle-Wells Syndrome | NBD | Local conformation | Buried |
| T438I | T434 | CINCA/NOMID Syndrome | WHD | HD2 interaction | Buried |
| A441V | A437 | | WHD | Local conformation | Buried |
| A441T | A437 | Muckle-Wells Syndrome | WHD | Local conformation | Buried |
| F525C | F523 | Muckle-Wells Syndrome | WHD | Local conformation | Buried |
| G571A | G569 | Muckle-Wells Syndrome | HD2 | Local conformation | Partially Buried |



Extended Data Fig. 8 | Mapping of the CAPS mutations on active NLRP3, and comparison of active NLRP3 and NLRC4. **a**, Locations of CAPS mutation sites on the active NLRP3 structure. Two views are shown. **b**, A list of the mutations, their domain location and potential structural effects. **c**, Superposition of the WHD from active NLRP3 (magenta) and inactive NLRP3 (PDB: 6NPY in grey), showing the formation of a β-hairpin in the active state. **d**, Superposition of the

WHD from active NLRP3 (magenta) and active NLRC4 (PDB: 3JBL in yellow), showing lack of the β-hairpin in NLRC4. **e**, Superposition of one NLRP3 subunit in two neighbouring NLRP3 subunits in a disk (coloured by domains) with one NLRC4 subunit in two neighbouring NLRC4 subunits in a disk (PDB: 3JBL in yellow). The second NLRC4 subunit needs to rotate by 31.7° to align with the second NLRP3 subunit.



Extended Data Fig. 9 | A structure-derived model for potential NEK7-independent, and LRR-deleted NLRP3 inflammasome activation. **a**, Under certain conditions such as those marked in the schematic (e.g. high NLRP3 expression level or certain effects from priming), monomeric NLRP3 or

destabilized caged NLRP3 may directly form the active NLRP3 disk with ASC upon stimulation. **b**, For overexpressed LRR-deleted NLRP3, stimulation would likely directly induce the activating conformational change to allow the assembly of the inflammasome disk with ASC.

Article

Extended Data Table 1 | Cryo-EM structure determination

| | NLRP3-NEK7 (decamer) | NLRP3 PYD filament |
|---|-------------------------|-----------------------|
| Data collection and processing | | |
| Nominal Magnification | 81,000 | |
| Voltage (keV) | 300 | |
| Electron exposure (e ⁻ /Å ²) | 50.4 | |
| Defocus range (μm) | -1.0 ~ -2.0 | |
| Pixel size (Å) | 1.06 | |
| Initial particle images (no.) | 808,941 | |
| Final particle images (no.) | 51,576 | 33,227 |
| Symmetry imposed | C10 | C3, Helical |
| Map resolution (Å) | 3.4 | 3.3 |
| FSC threshold | 0.143 | 0.143 |
| Map resolution range (Å) | 2.8-6.0 | 3.0-5.0 |
| Refinement | | |
| Initial model used | 6NPY/2WQM AlphaFold | 3QF2 |
| Model resolution (Å) | 3.4/3.9 | 3.3/3.6 |
| FSC threshold | (0.143/0.5) | (0.143/0.5) |
| Model resolution range (Å) | 60-3.4 | 60-3.3 |
| Map sharpening <i>B</i> factor (Å ²) | -112 | -125.7 |
| Model composition | | |
| Non-hydrogen atoms | 100,240 | 16,359 |
| Protein residues | 11,110 | 1995 |
| Ligands | 20 | 0 |
| <i>B</i> -factors(Å ²) | | |
| Protein | 142.08 | 144.42 |
| Ligand | 106.62 | |
| R.m.s. deviations | | |
| Bond lengths (Å) | 0.004 | 0.004 |
| Bond angles (°) | 0.693 | 0.943 |
| Validation | | |
| MolProbity score | 2.93 | 2.03 |
| Clashscore | 55.44 | 10.38 |
| Poor rotamers (%) | 1.95 | 0 |
| Ramachandran Plot | | |
| favoured (%) | 92.15 | 91.86 |
| allowed (%) | 6.94 | 8.09 |
| disallowed (%) | 0.91 | 0.05 |

Data collection, refinement, and validation statistics are shown.

Reporting Summary

Nature Portfolio wishes to improve the reproducibility of the work that we publish. This form provides structure for consistency and transparency in reporting. For further information on Nature Portfolio policies, see our [Editorial Policies](#) and the [Editorial Policy Checklist](#).

Statistics

For all statistical analyses, confirm that the following items are present in the figure legend, table legend, main text, or Methods section.

n/a Confirmed

- The exact sample size (n) for each experimental group/condition, given as a discrete number and unit of measurement
- A statement on whether measurements were taken from distinct samples or whether the same sample was measured repeatedly
- The statistical test(s) used AND whether they are one- or two-sided
Only common tests should be described solely by name; describe more complex techniques in the Methods section.
- A description of all covariates tested
- A description of any assumptions or corrections, such as tests of normality and adjustment for multiple comparisons
- A full description of the statistical parameters including central tendency (e.g. means) or other basic estimates (e.g. regression coefficient) AND variation (e.g. standard deviation) or associated estimates of uncertainty (e.g. confidence intervals)
- For null hypothesis testing, the test statistic (e.g. F , t , r) with confidence intervals, effect sizes, degrees of freedom and P value noted
Give P values as exact values whenever suitable.
- For Bayesian analysis, information on the choice of priors and Markov chain Monte Carlo settings
- For hierarchical and complex designs, identification of the appropriate level for tests and full reporting of outcomes
- Estimates of effect sizes (e.g. Cohen's d , Pearson's r), indicating how they were calculated

Our web collection on [statistics for biologists](#) contains articles on many of the points above.

Software and code

Policy information about [availability of computer code](#)

| | |
|-----------------|--|
| Data collection | Cryo-EM data collection: SerialEM (version 3.8). |
| Data analysis | Cryo-EM data analysis: MotionCor2 (version 1.1.0), Relion (version 3.08), Coot (version 0.8.9), PHENIX (version 1.17.1). Sequence alignment: Clustal Omega (accessed through the EMBL-EBI server). Molecular Graphics: UCSF ChimeraX (version 1.4) and PyMOL (version 2.5.2). Immunoblot quantification: ImageJ (version 1.51). Data plotting: OriginLab (OriginPro 2017 Suite). |

For manuscripts utilizing custom algorithms or software that are central to the research but not yet described in published literature, software must be made available to editors and reviewers. We strongly encourage code deposition in a community repository (e.g. GitHub). See the Nature Portfolio [guidelines for submitting code & software](#) for further information.

Data

Policy information about [availability of data](#)

All manuscripts must include a [data availability statement](#). This statement should provide the following information, where applicable:

- Accession codes, unique identifiers, or web links for publicly available datasets
- A description of any restrictions on data availability
- For clinical datasets or third party data, please ensure that the statement adheres to our [policy](#)

Atomic coordinates of the 10-fold, 11-fold and 4-subunit NLRP3-NEK7 assembly structures and NLRP3 PYD filament have been deposited in the PDB under accession numbers 8EJ4, 8EJ2 8EIV and 8ERT, respectively. The corresponding cryo-EM density maps have been deposited in the Electron Microscopy Data Bank under accession numbers EMD-28175, EMD-28173 EMD-28166 and EMD-28560, respectively. All other data are available from the corresponding authors upon reasonable request. Several structural coordinates in the PDB database were used in this study, which can be located by accession numbers 2WQM, 3J63, 3QF2, 6NPY, 7VTP, 7PZC, 7ZGU, 7ALV, 7PZD.

Human research participants

Policy information about [studies involving human research participants and Sex and Gender in Research](#).

Reporting on sex and gender

Use the terms sex (biological attribute) and gender (shaped by social and cultural circumstances) carefully in order to avoid confusing both terms. Indicate if findings apply to only one sex or gender; describe whether sex and gender were considered in study design whether sex and/or gender was determined based on self-reporting or assigned and methods used. Provide in the source data disaggregated sex and gender data where this information has been collected, and consent has been obtained for sharing of individual-level data; provide overall numbers in this Reporting Summary. Please state if this information has not been collected. Report sex- and gender-based analyses where performed; justify reasons for lack of sex- and gender-based analysis.

Population characteristics

Describe the covariate-relevant population characteristics of the human research participants (e.g. age, genotypic information, past and current diagnosis and treatment categories). If you filled out the behavioural & social sciences study design questions and have nothing to add here, write "See above."

Recruitment

Describe how participants were recruited. Outline any potential self-selection bias or other biases that may be present and how these are likely to impact results.

Ethics oversight

Identify the organization(s) that approved the study protocol.

Note that full information on the approval of the study protocol must also be provided in the manuscript.

Field-specific reporting

Please select the one below that is the best fit for your research. If you are not sure, read the appropriate sections before making your selection.

Life sciences

Behavioural & social sciences

Ecological, evolutionary & environmental sciences

For a reference copy of the document with all sections, see nature.com/documents/nr-reporting-summary-flat.pdf

Life sciences study design

All studies must disclose on these points even when the disclosure is negative.

Sample size

Sample sizes were not pre-determined. Cryo-EM images were collected until structures of satisfactory quality were solved, which suggested sufficient sample size. For biochemical and cellular experiments, no information was derived about a population based on sampling, and therefore sample size determination was not necessary.

Data exclusions

In cryo-EM processing, we discarded "junk" particles that could not be classified into useful 3D reconstructions. This is a widely used and accepted practice in the cryo-EM field. No other data were excluded from analysis.

Replication

All experiments were performed independently at least two or three times with similar results, as described in the figure legends.

Randomization

Proteins and cells were randomly allocated to the wells in each experimental group. Other randomization of experimental groups was not relevant to this study, and independent variables were controlled and did not require randomization.

Blinding

Blinding was not performed as subjective analysis was not needed. Each experiment was analyzed using consistent methods. Random allocation and quantitative measurements using various approaches and reaction kits as described in the methods minimized biased assessments.

Reporting for specific materials, systems and methods

We require information from authors about some types of materials, experimental systems and methods used in many studies. Here, indicate whether each material, system or method listed is relevant to your study. If you are not sure if a list item applies to your research, read the appropriate section before selecting a response.

Materials & experimental systems

| | |
|-----|---|
| n/a | <input type="checkbox"/> Involved in the study <input checked="" type="checkbox"/> Antibodies <input type="checkbox"/> Eukaryotic cell lines <input checked="" type="checkbox"/> Palaeontology and archaeology <input checked="" type="checkbox"/> Animals and other organisms <input checked="" type="checkbox"/> Clinical data <input checked="" type="checkbox"/> Dual use research of concern |
|-----|---|

Methods

| | |
|-----|--|
| n/a | <input type="checkbox"/> Involved in the study <input checked="" type="checkbox"/> ChIP-seq <input checked="" type="checkbox"/> Flow cytometry <input checked="" type="checkbox"/> MRI-based neuroimaging |
|-----|--|

Antibodies

Antibodies used

Mouse anti-NLRP3 (1:2000, Adipogen, Cat. no: AG-20B-0014-C100), mouse anti-β-actin (1:2,000, Sigma Aldrich, Cat. no: A2228-100UL) and rabbit anti-p20 of caspase-1 (1:1,000, Cell Signaling, Cat. no: 89332S) primary antibodies, respectively. Anti-mouse-HRP (1:5000, Cell Signaling, Cat. no: 7076S) and anti-rabbit-HRP (1:2,500, Cell signaling, Cat. no: 7074S) secondary antibodies were used.

Validation

All antibodies used in this study are commercially available and have been validated by the manufacturers' and/or previous publications.

Eukaryotic cell lines

Policy information about [cell lines and Sex and Gender in Research](#)

Cell line source(s)

NLRP3 KO iBMDM was a kind gift by Kate Fitzgerald
 Expi293F™ Cells <https://www.thermofisher.com/order/catalog/product/A14527>
 BL21(DE3) from Agilent [https://www.agilent.com/en/product/protein-expression/competent-cells-for-routine-proteinexpression/general-protein-expression/bl21\(de3\)-competent-cells-232943](https://www.agilent.com/en/product/protein-expression/competent-cells-for-routine-proteinexpression/general-protein-expression/bl21(de3)-competent-cells-232943)

Authentication

Cell lines were verified by manufacturer's website and Identity of these cell lines were frequently checked by their morphological features

Mycoplasma contamination

All cell lines were tested to be mycoplasma-negative by PCR.

Commonly misidentified lines (See [ICLAC](#) register)

No commonly misidentified cell lines are used in this study.